

Multi-agent reinforcement learning for the control of three-dimensional Rayleigh–Bénard convection

Joel Vasanth^{1*}, Jean Rabault², Francisco Alcántara-Ávila¹,
Mikael Mortensen³, Ricardo Vinuesa^{1*}

¹FLOW, Engineering Mechanics, KTH Royal Institute of Technology,
Stockholm, Sweden.

²Independent Researcher, Oslo, Norway.

³Department of Mathematics, University of Oslo, Oslo, Norway.

*Corresponding author(s). E-mail(s): jvasanth@kth.se;
rvinuesa@mech.kth.se;

Abstract

Deep reinforcement learning (DRL) has found application in numerous use-cases pertaining to flow control. Multi-agent RL (MARL), a variant of DRL, has shown to be more effective than single-agent RL in controlling flows exhibiting locality and translational invariance. We present, for the first time, an implementation of MARL-based control of three-dimensional Rayleigh–Bénard convection (RBC). Control is executed by modifying the temperature distribution along the bottom wall divided into multiple control segments, each of which acts as an independent agent. Two regimes of RBC are considered at Rayleigh numbers $Ra = 500$ and 750 . Evaluation of the learned control policy reveals a reduction in convection intensity by 23.5% and 8.7% at $Ra = 500$ and 750 , respectively. The MARL controller converts irregularly shaped convective patterns to regular straight rolls with lower convection that resemble flow in a relatively more stable regime. We draw comparisons with proportional control at both Ra and show that MARL is able to outperform the proportional controller. The learned control strategy is complex, featuring different non-linear segment-wise actuator delays and actuation magnitudes. We also perform successful evaluations on a larger domain than used for training, demonstrating that the invariant property of MARL allows direct transfer of the learnt policy.

Keywords: Reinforcement Learning, Active Flow Control, Rayleigh–Bénard Convection, Multi-agent Reinforcement Learning, Machine Learning

1 Introduction

Reinforcement learning (RL) is a data-driven approach to the problem of goal-directed sequential decision making. The RL framework involves an ‘agent’, which is its decision-making component, that learns a mapping from states to actions, called the ‘policy’, via a series of trial-and-error interactions with the environment. A reward signal, which is a scalar measure of performance of the environment in relation to the pre-defined goal, is fed back to the agent and is used in the optimization. The state S_t , action A_t and reward R_t form the three fundamental channels of communication between the agent and the environment. Each state is assigned a value $V(s)$ which is the expected total reward that can be obtained by that state in the long run, *i.e.*, $V(s) = \mathbb{E} [\sum_{k=0}^{\infty} \gamma^k R_{t+k+1} | s]$ (Sutton and Barto, 2018). The goal of the RL problem, then, is to maximise expected cumulative rewards or ‘returns’. In Deep RL (DRL), function approximators such as neural networks are used to parameterise either the policy, the value function, or both, which are updated during training via interaction with the environment in order to maximise the returns. Various solution methods have been developed to perform this optimisation, namely: (i) value-based methods such as Q-learning method (Van Hasselt et al., 2016; Mnih et al., 2013), where the value function is approximated and actions are chosen based on the approximated value function, (ii) policy-based methods (Silver et al., 2014), such as the policy gradient method, where the optimal policy is learned directly, and (iii) actor-critic methods such as the proximal policy optimisation (PPO) method (Schulman et al., 2017), where the critic network computes an advantage function to determine how good an action is compared to the average of all possible actions, given a state. Then, the actor network is updated based on the value of this advantage function. During training, interaction between the agent and the environment occurs on an episode basis, where an ‘episode’ is a single trajectory of the environment for a given fixed duration. Training is performed through trial-and-error that involves a stochastic exploration of the environment’s states, *i.e.*, selecting actions other than those dictated by the latest updated policy, which can improve the estimation of the state values. After training, the agent is evaluated on the environment in a deterministic manner according to the optimal policy, without exploration.

DRL is well adapted to perform control of complex, high-dimensional, nonlinear systems. A successful application that contributed to its recent popularity is in gaming, where neural network-based agents are trained to play and win computer games such as Atari (Mnih et al., 2013), Go (Silver et al., 2018) and Starcraft (Vinyals et al., 2019). DRL has also been applied to industrial control problems (Degraeve et al., 2022), biomechanical optimization problems (Verma et al., 2018), and recently, a number of classical active flow control (AFC) problems (Guastoni et al., 2023; Sonoda et al., 2022; Vignon et al., 2023; Font et al., 2024). Compared to traditional control methods that are used in AFC, such as state-space methods and adjoint methods (Chevalier, 2002), DRL does not require information about the governing equations or insight into the full state of the system. Even though there are a number of other techniques that aim at performing similar tasks as DRL (Brunton and Noack, 2015; Brunton et al., 2020; Pino et al., 2023), DRL has been found to be particularly flexible and effective in the recent years. While the trial-and-error learning method used in DRL can make it more

data-hungry and computationally expensive to train, once trained, predicting the next action from the learned approximation to the optimal policy is computationally cheap. This, in conjunction with the fact that DRL can be adapted to large state spaces, makes it a viable option for real-world control applications, such as AFC.

As a consequence, DRL for AFC has been the focus of much work over the last few years. One of the first uses of DRL in AFC was for the stabilisation of the vortex street in the flow past a two-dimensional (2D) cylinder at a low Reynolds number (Re) of 100 (Rabault et al., 2019; Rabault and Kuhnle, 2019). Here, the Reynolds number is given as $Re = \tilde{U}\tilde{H}/\tilde{\nu}$, where the symbols \tilde{U} , \tilde{H} and $\tilde{\nu}$ are the mean flow velocity, characteristic length scale of the system and kinematic viscosity respectively, and tilde $\tilde{\cdot}$ represents dimensional quantities. With two synthetic jets as the actuators, the drag was reduced by 8% and the learned control strategy was found to reduce pressure drop across the cylinder by increasing the area of the separated region. Following this study, DRL was applied to different configurations of the 2D cylinder. In Tang et al. (2020), four synthetic jets were used as DRL controllers for a wider Re range, $Re = 100-400$, and a maximum drag reduction of $\approx 38\%$ was achieved. Drag reduction was observed for unseen values of Re as well, showing the robustness of the DRL control process. The work by Ren et al. (2021) extends these studies to nonlinear unsteady conditions at $Re = 1000$, showing a reduction in drag by 30% along with a reduction of turbulent fluctuations. Varela et al. (2022) shows that a transition in the actuation strategy is obtained when the Reynolds number is further increased and turbulent stresses play a dominating role. Fan et al. (2020) and Xu et al. (2020) use a pair of smaller downstream rotating cylinders as actuators with a combined objective of drag reduction over the main cylinder and also to reduction of power loss due to cylinder rotation. More recently, an application to three-dimensional (3D) cylinders was studied in the Re range of 100 – 400 (Suárez et al., 2023), where again, DRL successfully showed a reduction of drag of $\approx 10\%$ for $Re = 400$. A number of studies have also considered questions related to the optimization of the full DRL control setup, including probe placement (Paris et al., 2023, 2021; Yan et al., 2023) and the use of time history from the state probes (Wang et al., 2024). Moreover, applications related to vortex induced vibration (Ren et al., 2019; Chen et al., 2023; Ren et al., 2024), or hydrodynamic stealth (Ren et al., 2021), have also attracted interest. Aside from the cylinder, other applications include the control of chaotic flows such as the flow arising from the Kuramoto–Sivashinsky (KS) equation (Bucci et al., 2019; Xu and Zhang, 2023), drag reduction in 3D channel flows (Guastoni et al., 2023; Sonoda et al., 2022), suppression of the instability of a one-dimensional (1D) falling liquid film (Belus et al., 2019), suppression of 2D Rayleigh–Bénard convection (RBC) (Beintema et al., 2020; Vignon et al., 2023) and other practical problems (Ren et al., 2019, 2021; Li and Zhang, 2022). We refer the interested reader to some comprehensive reviews of DRL applied to flow control (Vinuesa et al., 2022; Vignon et al., 2023; Rabault et al., 2020; Garnier et al., 2021) for more detail. This rapid development has been made possible largely thanks to both the availability of open source DRL frameworks that make it easy to deploy advanced DRL algorithms (Kuhnle et al., 2017a; Guadarrama et al., 2018), and open source computational fluid dynamics (CFD) tools (Alnæs et al., 2015;

Jasak et al., 2007). These are being increasingly merged into turn-key frameworks that make it easy to start applying DRL to CFD simulations (Wang et al., 2022).

In relation to the works described above, several associated challenges have been solved over the last few years. For example, Rabault and Kuhnle (2019) have leveraged a multi-environment DRL framework where several numerical simulations run in parallel, each providing its own set of S_t , A_t and R_t to a common agent, therefore scaling up the number of experiences. With their approach, they showed that speedups in training are obtained proportional to the number of simultaneous environments used. The study by Belus et al. (2019) introduced a multi-agent RL (MARL) framework for the control of flow systems with distributed inputs and outputs. MARL was since then repeatedly proved to be effective in problems where the dynamics of the system are translationally invariant in space and multiple actuators are required to control the system, *i.e.*, the control dimensionality is large. With a single-agent RL (SARL) framework, this large dimensionality would result in the curse of dimensionality on the action dimension making learning impractical. In the MARL framework, each agent is defined by separate streams of states, actions and rewards, each unique to a single agent. Moreover, critically, all agents share a common parameterisation, *i.e.*, the same neural network weights. Note that here, we consider one of several possible configurations of MARL. An alternative MARL configuration, is where each agent has different individual parameterisations, and they are used to learn policies for different sub-tasks which contribute to a common goal. We refer the interested reader to the details of several such MARL variants in Albrecht et al. (2024). In the present work, each agent observes a small subdomain of the full domain, which we define as a ‘pseudo-environment’ (Sec. 2.3), and is thus responsible for only a subset of the total number of control actions, thereby overcoming the curse of dimensionality. The use of a common agent parameterisation is justified by the fact that the governing equations (and thus the qualitative features of the flow dynamics) are invariant over all pseudo-environments, and experience can be shared among MARL agents. Following Belus et al. (2019), recent works that employ MARL and have demonstrated its effectiveness are Guastoni et al. (2023) for the control of 3D turbulent channels, Suárez et al. (2023, 2024) to reduce drag over a 3D cylinder, Novati et al. (2021); Bae and Koumoutsakos (2022) for turbulence closure modelling and Vignon et al. (2023) for the control of 2D RBC, to name a few.

The present work is an extension to 3D of the previous application of MARL to RBC in 2D presented by Vignon et al. (2023). The RBC phenomenon is a fundamental problem widely studied academically in the field of thermally driven flow instabilities (Drazin and Reid, 2004), which is also found in a range of natural phenomena and industrial applications. In our configuration, the domain consists of a fluid layer of height \tilde{H} bounded by two rigid walls, where the temperature at the bottom wall \tilde{T}_H is maintained at a constant value higher than the top wall temperature \tilde{T}_C . This forms an adverse temperature gradient $\Delta\tilde{T}/\tilde{H} = (\tilde{T}_H - \tilde{T}_C)/\tilde{H}$, which at a certain large enough value, destabilises the system. The instability occurs due to competing driving and damping effects, the driving effect being the vertical adverse thermal gradient and the damping effect being viscosity (Bergé and Dubois, 1984). The stability is governed by a non-dimensional number, the Rayleigh number Ra, which is the ratio of the time

scales of heat transport by conduction and by convection. The Rayleigh number is expressed as $Ra = \tilde{g}\tilde{\alpha}_T\Delta\tilde{T}\tilde{H}^3/(\tilde{\nu}\tilde{\kappa})$, where \tilde{g} stands for the acceleration due to gravity, $\tilde{\alpha}_T$ is the thermal expansion coefficient and $\tilde{\kappa}$ is the thermal diffusivity. At a certain critical $Ra = Ra_c$, instability occurs via a supercritical bifurcation from the no-motion purely conductive state to the convective state (Getling, 1998). At large $Ra > Ra_c$, the heat transfer from the bottom wall to the top wall is dominated by convection. Another useful dimensionless number is the Nusselt number Nu , which is defined as the ratio of the combined convective and conductive heat flux to the heat flux due to conduction alone. The Nusselt number is given as $Nu = 1 + \sqrt{Ra Pr} \langle vT \rangle_{x,y,z}$, where Pr is the Prandtl number ($Pr = \tilde{\nu}/\tilde{\kappa}$), v and T are non-dimensional vertical velocity and temperature and $\langle \cdot \rangle_{x,y,z}$ represents averaging over the entire domain. The manner of non-dimensionalisation is detailed in Sec. 2.1.

Several approaches have been used to suppress the magnitude of convection in RBC systems. Passive flow control techniques (Kelly, 1992; Carbo et al., 2014; Swaminathan et al., 2018) have shown only minor improvements in delaying the onset of convection (*i.e.*, increasing the Ra_c). Active flow control techniques have proven to be more successful. Several AFC techniques involve modulation of the bottom wall temperature distribution (Singer and Bau, 1991; Wang et al., 1992; Or and Speyer, 2003; Howle, 1997; Remillieux et al., 2007; Tang and Bau, 1993).

The first application of DRL to RBC was presented by Beintema et al. (2020) in a 2D domain using the single-agent RL framework. They studied the control of RBC in a square domain confined by no-slip walls with the lateral walls being adiabatic, top wall being isothermal, and temperature control modulation imposed on the bottom wall. The Ra_c at which convection occurs was reduced as the DRL controller converted a single-cell configuration in the uncontrolled system to a vertically stacked double cell configuration, reducing the effective Ra . In a following study by Vignon et al. (2023), the MARL framework was used on a domain with periodic boundary conditions on the lateral walls, featuring two convection cells in the uncontrolled state. Given that MARL is advantageous for problems with distributed inputs and outputs for which invariants are observed, a superior performance compared to SARL was demonstrated, in terms of faster learning. MARL achieved a 22.7% reduction in Nu , employing a control strategy that coalesces the two convection cells into a single-cell state, thus reducing the convection intensity. By extension to Beintema et al. (2020) and Vignon et al. (2023), in the present study, the RBC system is three-dimensional. Therefore, the actuators are now two-dimensional surfaces at the bottom of the 3D fluid domain, as opposed to one-dimensional segments at the bottom of a 2D domain. As a consequence, in order to match the necessity to cover a 2D surface with actuators, the number of actuators is increased from 10 in Vignon et al. (2023) to $8 \times 8 = 64$ in the present case. If we consider a single-agent RL approach, this would mean that the action produced by the DRL agent would be a vector of 64 values, leading to the curse of dimensionality (Belus et al., 2019; Vignon et al., 2023). This further motivates the need for the MARL framework for the execution of control in 3D. As far as the authors' knowledge of the past literature goes, the present study is the first application of MARL to 3D RBC.

In particular, the main contributions of the present work are the following:

- We introduce the MARL framework for 3D RBC. In 3D, the control dimensionality is multiplicatively larger, therefore, the use of multiple local agents corresponding to a MARL setup is much preferred to the SARL setup. Two cases of Rayleigh numbers, $Ra = 500$ and $Ra = 750$, are tested.
- We show that MARL is successful in reducing convection at both Ra regimes. The MARL controller drives the system from an uncontrolled state with irregular unsteady convection rolls, to a controlled state with regularly arranged steady convection rolls. The regularly arranged convection rolls are similar to the shape of convection structures found at a lower Ra than $Ra = 500$ and $Ra = 750$. Given that the Ra is representative of the regime of instability (Bergé and Dubois, 1984), with flows at lower Ra being relatively less unstable than flows at higher Ra , we make it evident that the MARL-controlled states at $Ra = 500$ and $Ra = 750$ resemble flow from a less unstable regime, *i.e.*, a regime at lower Ra .
- We demonstrate how MARL can exploit translational invariances to obtain transferable strategies, by testing a pre-trained agent trained at $Ra = 500$ on a domain of larger size. We show that MARL reduces convection on the larger-size domain as well, without any additional tuning or modification of the agent.
- We apply classical proportional control and compare the performance of the MARL controller against the proportional controller. The MARL controller is shown to provide a larger reduction in Nu than the proportional controller in both Ra cases studied.

The rest of the paper is organised as follows. Sec. 2 provides a detailed description and formulation of the RBC problem (Sec. 2.1), the numerical methods used for the CFD (Sec. 2.2), and a description of the DRL control (Sec. 2.3) and proportional control (Sec. 2.4) methods. In the results section, Sec. 3, the uncontrolled states are described in Sec. 3.1, and results from the training are discussed in 3.2. The evaluation of the trained agent in deterministic mode is provided in Sec. 3.3 and results of deterministic evaluation in a larger domain are provided in Sec. 3.5. Proportional control is discussed in Sec. 3.4. We conclude the paper in Sec. 4. Multimedia (video) files are referred to in the caption of various figures in the text and information about these is provided in the ‘Supplementary Information’ section in Appendix B. We release the full code used in this study as open source materials, and the relevant information is provided in Appendix C.

2 Formulation and Methodology

2.1 RBC Formulation

The formulation of the RBC problem closely follows that of Vignon et al. (2023). The governing equations are the Navier–Stokes equations under the Boussinesq approximation, commonly adopted for convection problems. The Boussinesq approximation states that the density variation is only important in the gravitational term and neglects it in the rest of the equation. The continuity equation then reduces to the incompressible form, which further simplifies the viscous terms in the momentum equation. The viscosity is also assumed to be a constant. The equations are then made

dimensionless by the domain height \tilde{H} , reference velocity $\tilde{U}_{\text{ref}} = \sqrt{\tilde{g}\tilde{\alpha}_T\Delta\tilde{T}\tilde{H}}$ and the temperature difference $\Delta\tilde{T} = \tilde{T}_H - \tilde{T}_C$ between the bottom and top walls. Note that dimensional quantities are indicated with the tilde $\tilde{\cdot}$. The variable \tilde{g} stands for the acceleration due to gravity, and $\tilde{\alpha}_T$ is the thermal expansion coefficient. Upon non-dimensionalisation, the coefficients can be refactored in terms of two non-dimensional constants, *i.e.*, the Rayleigh number $\text{Ra} = \tilde{g}\tilde{\alpha}_T\Delta\tilde{T}\tilde{H}^3/(\tilde{\nu}\tilde{\kappa})$ and Prandtl number $\text{Pr} = \tilde{\nu}/\tilde{\kappa}$. The variable $\tilde{\nu}$ is the kinematic viscosity and $\tilde{\kappa}$ is the thermal diffusivity. Denoting the unit vectors in the x , y and z directions as \mathbf{i}, \mathbf{j} and \mathbf{k} respectively, the governing equations are (Pandey et al., 2018):

$$\nabla \cdot \mathbf{u} = 0, \quad (1a)$$

$$\frac{\partial \mathbf{u}}{\partial t} + (\mathbf{u} \cdot \nabla) \mathbf{u} = -\nabla p + \sqrt{\frac{\text{Pr}}{\text{Ra}}} \nabla^2 \mathbf{u} + T \mathbf{j}, \quad (1b)$$

$$\frac{\partial T}{\partial t} + \mathbf{u} \cdot \nabla T = \frac{1}{\sqrt{\text{Ra Pr}}} \nabla^2 T. \quad (1c)$$

The velocity vector $\mathbf{u}(x, y, z, t)$ comprises of the three velocity components $\mathbf{u} = u\mathbf{i} + v\mathbf{j} + w\mathbf{k}$, and $T(x, y, z, t)$ is the temperature. The computational domain is cuboidal in shape with coordinates x and z representing horizontal directions and y representing the vertical direction. The variable t represents time. The length L of the domain is measured along x and z and the height H along y . The domain extends in the horizontal direction as $x, z \in [0, L]$ and in the vertical direction as $y \in [-1, 1]$. Note that in this work, $L = 4\pi$ and $H = 2$. A schematic representation of the domain is shown in Fig. 1. To set up the temperature gradient, the top wall is at all times maintained at a spatially uniform temperature of 1, *i.e.*, $T_C = T(x, y = 1, z, t) = 1$. The bottom wall is allowed to have a spatial distribution, *i.e.*, $T_H(x, z, t) = T(x, y = -1, z, t) \neq \text{constant}$, but we enforce that the spatial mean, *i.e.*, $\langle T_H(x, z, t) \rangle_{x,z} = T_{H,0}$, is equal at all time to 2. The operator $\langle \cdot \rangle$ represents averaging in space. Note that T_H is also spatially uniform during the uncontrolled simulations, *i.e.*, $T_H(x, z, t) = 2$, and it is only during the control simulations that the constant mean temperature constraint is enforced at the bottom wall. For the initial condition, a constant temperature gradient is provided as the temperature field, and quiescent flow for the velocity field. Periodic boundary conditions for velocity and temperature are provided at the lateral boundaries, while a no-slip boundary condition is prescribed at the top and bottom walls, along with the isothermal $T_C = 1$ boundary at the top wall and constant $T_{H,0} = 2$ at the bottom wall.

A useful dimensionless number that can be used to quantify the magnitude of convection is the Nusselt number Nu . The Nu is defined as the ratio between the combined heat fluxes due to convection and conduction, and the heat flux due to conduction alone (Pandey et al., 2018):

$$\text{Nu}(t) = 1 + \sqrt{\text{Ra Pr}} \langle vT \rangle_{x,y,z}. \quad (2)$$

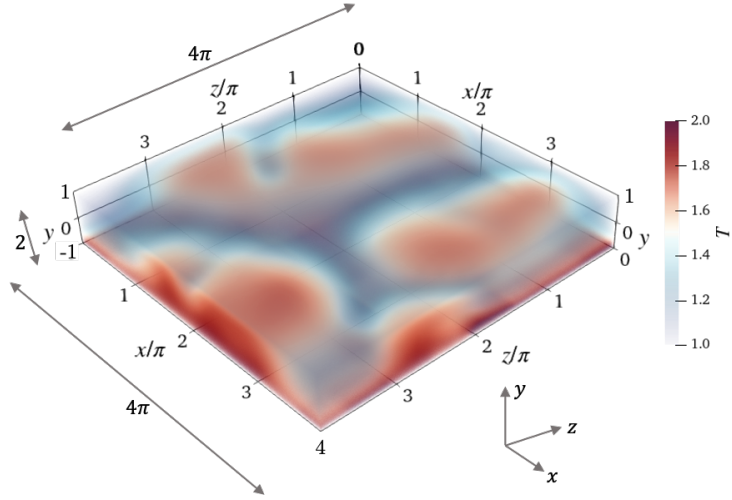


Fig. 1 Illustration of the computational domain used in the simulation of the RBC system with its dimensions. Shown is the instantaneous temperature field along with convection rolls that form in the system as a result of the RB instability.

2.2 Numerical Method for the CFD

Following [Vignon et al. \(2023\)](#), the governing equations (1) along with boundary conditions are implemented with a spectral Galerkin method using a technique developed by [Kim et al. \(1987\)](#) for direct numerical simulations of turbulent channel flows. In this method the pressure is eliminated and the 3D Navier–Stokes equations are basically reduced to the continuity equation, a fourth-order equation for the wall-normal velocity component and a second-order equation for the wall-normal vorticity component. Adding the energy equation, the four scalar equations that are solved are Eqs. (1a), (1c), as well as:

$$\frac{\partial \nabla^2 v}{\partial t} = \frac{\partial^2 H_x}{\partial x \partial y} + \frac{\partial^2 H_z}{\partial z \partial y} - \frac{\partial^2 H_y}{\partial x^2} - \frac{\partial^2 H_y}{\partial z^2} + \sqrt{\frac{\text{Pr}}{\text{Ra}}} \nabla^4 v + \frac{\partial^2 T}{\partial x^2} + \frac{\partial^2 T}{\partial z^2}, \quad (3)$$

$$\frac{\partial g}{\partial t} = \sqrt{\frac{\text{Pr}}{\text{Ra}}} \nabla^2 g + \frac{\partial H_x}{\partial z} - \frac{\partial H_z}{\partial x}, \quad (4)$$

where $\mathbf{H} = (\mathbf{u} \cdot \nabla) \mathbf{u}$ is the convection vector and $g = (\nabla \times \mathbf{u}) \cdot \mathbf{j}$ is the normal vorticity component. The initial condition for the temperature is a linear gradient in the y -direction with the bottom and top wall temperatures maintained at 2 and 1 respectively. Equation (3) is implemented with the four boundary conditions $v(x, \pm 1, z, t) = v'(x, \pm 1, z, t) = 0$, where the first two are due to no slip, whereas the two latter follow from the continuity equation. Equation (4) is derived by taking the curl of (1b), and the y -component g is subsequently solved with $g(x, \pm 1, z, t) = 0$ (no slip). Periodic boundary conditions in the x and z directions are applied between

the lateral boundaries, and this is implemented through the choice of the numerical elements and basis functions, as described below.

The four scalar equations (1a), (1c), (3) and (4) are implemented using a highly-accurate spectral Galerkin discretization in space (Shen et al., 2011) and a third-order implicit/explicit (IMEX) Runge-Kutta method (Ascher et al., 1997) for the temporal integration. The Galerkin method makes use of tensor product basis functions constructed from Chebyshev polynomials for the wall-normal y direction and Fourier exponentials for the periodic directions x and z . The boundary conditions in both directions are built into the basis functions and as such enforced exactly. For the wall-normal direction this requires the use of composite Chebyshev polynomials (Shen et al., 2011), whereas the Fourier exponentials for the x -direction are already periodic. Since the continuity equation cannot be used to find u for Fourier wavenumber 0, we solve for this wavenumber the momentum equation in the x direction. All other unknowns are closed through Eqs. (1a), (1c), (3) and (4). The convection terms \mathbf{H} and $\mathbf{u} \cdot \nabla T$ are computed in physical space after expanding the number of collocation points by a factor of 3/2 in order to avoid aliasing. For \mathbf{H} we use the rotational form $\mathbf{H} = -\mathbf{u} \times (\nabla \times \mathbf{u})$, with the remaining $1/2 \nabla \mathbf{u} \cdot \mathbf{u}$ absorbed by the pressure, and for temperature we use the divergence form $\mathbf{u} \cdot \nabla T = \nabla \cdot \mathbf{u} T$.

The code is implemented using the open-source spectral Galerkin framework ‘shenfun’ (Mortensen, 2018a), where the equations can be automatically discretized through a high-level scripting language closely resembling the Mathematics. The Navier–Stokes solver has been verified by reproducing the growth of the most unstable eigenmode of the Orr–Sommerfeld equations over long time integrations. The Navier–Stokes and Rayleigh–Bénard solvers are distributed as part of the shenfun software, and there is a demonstration guide published in the documentation (Mortensen, 2018b), which also provides a much more detailed description of the numerical method. Links are provided in Appendix C, and we refer the reader interested in all the technicalities of the numerical solver implementation to the resources detailed therein.

The observation probes are distributed over the domain as a uniform mesh. For purposes of illustration, probes over four randomly selected segments (to avoid overcrowding) are shown in black dots in Fig. 2. There are $32 \times 8 \times 32$ total probe-mesh points in the x , y and z directions, respectively. The number of quadrature points in the solution approximation used by the spectral Galerkin solver is equal to the number of Galerkin modes, which is $32 \times 16 \times 32$. The resulting solution is spatially continuous, and the observations are then evaluated from these global, continuous spectral Galerkin functions at the uniform mesh probe locations. These observations are used in the DRL-based control methodology which we describe next.

2.3 DRL Control Methodology

The numerical simulations is solved with the methods described in the previous section from the constant temperature gradient initial condition up to a time instant when the time-averaged Nu, \overline{Nu} , becomes statistically constant and the RBC flow structures are fully-developed. By ‘fully-developed’, we mean that the flow variables u , v , w and T (and by consequence, Nu) are statistically stationary. Note that the overbar denotes averaging with respect to time. The \overline{Nu} averaged over the last half of the

total baseline simulation time is denoted as Nu_{ref} , which is the reference Nu used in the reward computation, as will be described later in this section. We refer to these uncontrolled initial simulations as the ‘baseline’, since states at the final instants of these simulations serve as initial conditions for the control. For $Ra = 500$, the time duration of the baseline is 400 time units and for $Ra = 750$ it is 5000.

The control is applied to the RBC system as temperature actuations on the bottom wall boundary at $y = -1$. The bottom wall boundary is divided into 8×8 square segments all of which are of equal size of $\pi/2 \times \pi/2$ in the x and z directions. The RBC system with the bottom wall segments together form the DRL environment. As mentioned in Sec. 1, DRL occurs via interactions between three fundamental channels of communication between the environment and the agent: the state S_t , action A_t and reward R_t at time t . As per the SARL framework, S_t comprises all the physical quantities measured at observation probes distributed within the domain, R_t is a measure based on the performance of the system, and A_t are the set of outputs from the agent which are control actuations. In the case of the RBC system S_t can, for example, be values of $[T, u, v, w]$ at the observation probes, R_t can be a function of Nu and A_t the set of 64 temperature actuations T_{act} applied on each segment.

In the following, we use a MARL setup as illustrated in Fig. 2. In MARL, N_{ag} multiple agents are each assigned to different local sections of the entire domain, which we refer to as ‘pseudo-environments’. We define a pseudo-environment as the block of the domain directly above each individual segment. Each agent is associated with its own stream of state, action and reward from its corresponding pseudo-environment which we denote as $s_t^{(j)}$, $a_t^{(j)}$ and $r_t^{(j)}$ respectively, $j = 1, \dots, N_{\text{ag}}$ being the agent index. Here, note the modification in notation from uppercase letters to lowercase letters: uppercase representing states, actions and rewards corresponding to the entire domain as per the SARL framework, and lowercase representing states, actions and rewards specific to each pseudo-environment as per the MARL framework. We represent segment-specific values with the superscript j in parenthesis. Note that the $r_t^{(j)}$ is a ‘weighted’ local reward, which is a combination of a ‘local’ and ‘global’ Nu as described below. This is based on the fact that the RBC environment is invariant in the horizontal directions x and z , so maximising a local reward can correspond to maximising the global reward in a cumulative manner. The state, action and reward tuples from each pseudo-environment and then from each timestep are batched together consecutively up to a size corresponding to the batch size, before an agent update is performed.

A key aspect of the MARL implementation that exploits translational invariance is that all the trainable weights in the agent parameterisation are shared, *i.e.*, all agents, defined by their separate streams of state, action and reward, share the same neural network. This is an effective way to share experience across the domain and alleviate the curse of dimensionality over the control space dimension, as previously highlighted in (Belus et al., 2019; Vignon et al., 2023).

The states $s_t^{(j)}$ from each pseudo-environment are obtained from a set of $4 \times 8 \times 4 = 128$ observation probes distributed with even spacing in the j^{th} pseudo-environment. A representation of this is shown in Fig. 2 within the RBC domain in four randomly selected pseudo-environments. Four physical quantities: temperature and

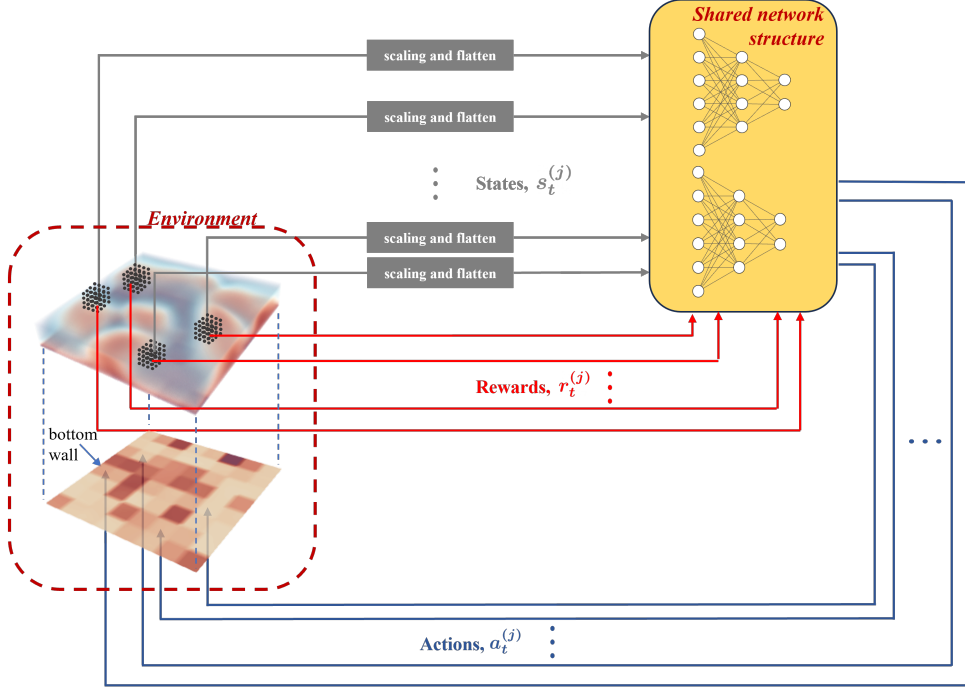


Fig. 2 An illustration of the MARL setup. The environment consists of the RBC system (top) with a projection of the bottom wall boundary (below) also shown. The bottom boundary is divided into N_{ag} square segments where temperature control actuations are applied. Observation probes are distributed uniformly throughout the domain, but for illustration purposes are depicted with black dots in blocks of the domain directly above four pseudo-environments. Each pseudo-environment along with their streams of actions, states and rewards form multiple agents. The index j represents the j^{th} agent, with $j = 1, \dots, N_{\text{ag}}$. All agents share the same neural network parameterisation in the PPO algorithm. A schematic of two networks are shown representing the actor and critic parameterisation.

three velocity components $[T, u, v, w]$ are observed from each probe in each pseudo-environment. A scaling or shifting is performed to ensure that the state values are roughly between -1 and 1 and not too small. The velocities are scaled as $u_s = 1.5 \times u$, $v_s = 1.5 \times v$ and $w_s = 1.5 \times w$ and the temperature is shifted as $T_s = T - 1.8$, where subscript s stands for ‘scaled’ or ‘shifted’. The scaling factors used are based on the range of values observed in the baseline so that the scaled variables are roughly within the range $[0, 1]$. These 512 quantities (4 variables measured at 128 observation probes) are flattened to form the local state vector $s_t^{(j)} = [T_s, u_s, v_s, w_s]^{(j)}$.

The goal of any DRL algorithm is formulated as a maximisation problem, *i.e.*, to maximise the reward. In the MARL framework, the definition of reward for the j^{th} pseudo-environment is slightly modified: it incorporates two Nu values, one calculated within the j^{th} MARL pseudo-environment called the local Nusselt number $\text{Nu}^{(j)}$, and one calculated over the entire domain called the global Nu. The global Nu is calculated

using Eq. (2). The local Nu, $\text{Nu}^{(j)}$, is given as:

$$\text{Nu}^{(j)}(t) = 1 + \sqrt{\text{Ra Pr}} \langle vT \rangle_{x^{(j)}, y, z^{(j)}}, \quad (5)$$

where $x^{(j)}$ and $z^{(j)}$ are the horizontal coordinate intervals corresponding to the j^{th} pseudo-environment, *i.e.*, in the j^{th} pseudo-environment. The global Nu is the part of the reward that accounts for the main goal of the agent, to minimise the convection over the entire channel. This incentivizes each pseudo-environment to improve the global flow state. The local Nu provides information to the agent about the local effects of the actions on the flow. This allows for more reward granularity to the agent during training. Given that the RBC control goal is to minimise Nu, we define the total reward for the j^{th} pseudo-environment to be a weighted reward $r_t^{(j)}$ proportional to the negative of a weighted sum of the global and local Nu, defined as:

$$r_t^{(j)} = \text{Nu}_{\text{ref}} - \left[\beta \text{Nu}^{(j)}(t) + (1 - \beta) \text{Nu}(t) \right], \quad (6)$$

where Nu_{ref} is the reference value equal to \overline{Nu} with time-averaging performed over the last half of the total baseline simulation time and the factor $\beta = 0.0015$ is a weighting factor determining the relative weight of the local and global Nu contained in the reward. From Eq. (6), a lower local or global Nu results in a higher reward. The value of β appears low, but this is due to the difference in geometric width used to compute the local and global Nu's. We choose β such that the local Nu accounts for about 10% contribution to the total reward.

The output from the agents are actions $a_t^{(j)}$ in the range between -1 and 1 , each agent generating a single action for its corresponding control segment. These actions are then transformed into temperature actuations $T_{\text{act}}^{(j)}$ applied to each bottom area using a shifting and normalisation process following:

$$a_t'^{(j)} = a_t^{(j)} - \frac{1}{N_{\text{ag}}} \sum_{j=1}^{N_{\text{ag}}} a_t^{(j)}, \quad (7)$$

$$K = \max \left(1, \max_j \left| a_t'^{(j)} \right| \right), \quad (8)$$

$$T_{\text{act}}^{(j)} = T_{H,0} + \Lambda \frac{a_t'^{(j)}}{K}. \quad (9)$$

In the above, each raw action is first subtracted by the mean over actions for all segments (*i.e.*, for each MARL agent) to form action perturbations $a_t'^{(j)}$. The value K is a factor to ensure that action perturbations larger than 1 are scaled down before being converted into temperatures. The factor Λ controls the magnitude of the temperature actuations. The above equations ensure that the mean temperature at the bottom boundary is kept at a constant value of $T_{H,0} = 2$. This is the constant mean temperature constraint as described in Sec. 2.1. The RBC flow regime is characterised by the Ra which depends on $T_{H,0}$, and thus changing $T_{H,0}$ would modify this regime.

Thus, the constant mean temperature constraint is to ensure that despite the application of the control values, the regime of the instability remains unmodified and the system is controlled within this regime.

The states, rewards and actions described above are implemented within the framework of the ‘Tensorforce’ library (Kuhnle et al., 2017b). Tensorforce contains several optimisation algorithms for reinforcement learning. In the present work, the widely used policy gradient method, proximal policy optimisation (PPO), is employed to train the agent. PPO is an actor-critic method where the actor approximates the policy distribution and the critic approximates the value function of the current state (Sutton and Barto, 2018). Both the policy and the critic are represented by neural networks.

We define an episode as a simulation spanning 200 actuations, each actuation lasting for 15 time steps. At this point, we make a distinction in terminology between two types of episodes used in the MARL framework: ‘CFD episodes’ and ‘MARL episodes’. Both are simulations spanning 200 actuations, however, the difference lies in the part of the domain considered in the simulation. A CFD episode is a simulation of the entire domain involving 200 sets of N_{ag} actuations, one set for each action step. A MARL episode considers only the 200 actuations as applied locally by a single pseudo-environment. Thus, the simulation of a single CFD episode implies that N_{ag} MARL episodes are simulated. All results in this paper are plotted with respect to CFD episodes only. Therefore, hereafter in the text and figures, the usage of the term ‘episode’ refers to ‘CFD episode’, unless otherwise specified. A set of other training hyperparameters used in this study is provided in Table 1.

In the present work, 200 and 400 total CFD episodes are simulated for $Ra = 500$ and $Ra = 750$ respectively, and each actuation in any given episode is applied for a duration of 15 timesteps. In order to ensure that the agent is also trained on states from longer simulations, we ensure that 20% of the episodes start from the end of the previous episode, and the remaining 80% starts from the end state of the baseline. In this way, the system also explores trajectories spanning a longer time across successive episodes durations, and thus the agent observes more states, including states representative of the long-term behavior of the system. We use a batch size of 3 CFD episodes (*i.e.*, $3 \times N_{\text{ag}} = 3 \times 64 = 192$ MARL episodes). We found that with lower batch sizes, training is largely unstable. We explain this observation as follows. Neural networks learn best from data that is uncorrelated. Since data from adjacent MARL environments is strongly (spatially) correlated, a batch size large enough must be chosen such that independent trajectories can be sampled during training. On the other hand, a batch size too large would make training sluggish. Other agent hyperparameters and CFD parameters are provided in Table 1. Training is performed with a discount factor of $\gamma = 0.99$. For details of the algorithmic implementation of MARL, we refer the interested reader to Vignon et al. (2023). We follow the same code implementation therein.

2.4 Proportional Control Methodology

We also employ a proportional controller in order to compare the performance of the DRL-based controller described in the previous section, for $Ra = 500$ and $Ra = 750$. For proportional control, actuations proportional to the temperature perturbations

are applied on the bottom wall segments. The size of the bottom wall segments and number of segments are the same as described in Sec. 2.3. In order to compute the magnitude of the temperature perturbations during instability, we require a reference temperature quantity from a stable state devoid of any RB instability. For this, we consider a low $Ra = 100$, corresponding to a stable regime that features a no-motion purely conductive state with a constant temperature gradient. The temperature at the mid-plane $y = 0$ is measured, and we denote the temperature averaged over the entire mid-plane as $T_{\text{ref},100} = \langle T(x, y = 0, z, t) \rangle_{x,z,t}$. We use $T_{\text{ref},100}$ as the reference temperature. Next, for $Ra = 500$ and $Ra = 750$, at each time instant of the simulation, the temperature perturbation T' is measured as

$$T'(x, z, t) = T_{\text{ref},100} - T(x, y = 0, z, t). \quad (10)$$

Note that the value of T' at the portion of the mid-plane directly above each control segment is used as the observation. For the j^{th} segment, the observation is $T'(x^{(j)}, z^{(j)}, t)$. A control action $T_p^{(j)}$ proportional to $-T'(x^{(j)}, z^{(j)}, t)$ is then applied on the j^{th} segment on the bottom wall as:

$$T_p^{(j)} = -K_p \langle T'(x^{(j)}, z^{(j)}, t) \rangle_{x^{(j)}, z^{(j)}}. \quad (11)$$

For the constant of proportionality K_p , a range of values is tested in both $Ra = 500$ and $Ra = 750$. For $Ra = 500$, the K_p range is from 0.1 to 1.0 in increments of 0.1. For $Ra = 750$, the range of K_p is 0.1 to 2.0 in increments of 0.1. A wider range is used for $Ra = 750$ since it is more unstable than $Ra = 500$ and may require a larger amplitude of control. The response of the system for each individual K_p is simulated with the initial condition being the end state of the baselines, until a controlled state is reached.

3 Results and Discussion

3.1 Baselines

Figure 3 shows the evolution of Nu in the baseline simulations of each of the cases $Ra = 500$ and $Ra = 750$. The value of the Nu begins at 1.0, indicating the initial condition, *i.e.*, the no-motion state where the heat transfer is due to conduction only. This state is unstable and the convective state sets in accompanied by a rise in Nu . Then, Nu stabilises at a given value or oscillates around a mean value, after which the baseline simulation is stopped.

For $Ra = 500$, five simulations were performed with the same parameters. The simulations all result in topologically similar solutions with similar Nu values. We show a single solution in Fig. 3(a). For $Ra = 750$, similarly, five simulations of the baseline were performed with identical simulation parameters. However, in contrast to $Ra = 500$, three different end-states are reached owing to the system chaoticity and stochasticity at $Ra = 750$, some of which are oscillatory and some of which are steady. Since Ra is higher, this state is more unstable and dynamically rich compared to $Ra = 500$. We classify these baselines into three classes, class 1 to class 3, based on the magnitudes of Nu after the transients have died away. The value of \overline{Nu} is the obtained

Table 1 Parameters used in the present study.

Parameter	Value
CFD	
Prandtl number, Pr	0.7
Time step, Δt	0.1
Domain size	$4\pi \times 2 \times 4\pi$
Number of Galerkin modes	$32 \times 16 \times 32$
Number of probes per pseudo-environment	$4 \times 8 \times 4$
DRL	
Number of CFD episodes for Ra = 500	200
Number of CFD episodes for Ra = 750	400
Actions per CFD episode	200
Action duration	15 time steps
Number of agents, N_{ag}	64
State size	512
Number of hidden layers (actor and critic networks)	2
Number of units per hidden layer (actor and critic networks)	128
Batch size	3 CFD episodes
Reward weighting factor, β	0.0015
Temperature actuation magnitude factor, Λ	0.9
Discount factor, γ	0.99
PPO clipping factor	0.2
Learning Rate	0.001
Entropy regularisation coefficient	0.01
Optimizer	Adam
Proportional Control	
Reference temperature, $T_{\text{ref},100}$	1.5

after time averaging Nu over the last half of the baseline time. Class 1 corresponds to run 4, which shows a value of $\overline{Nu} = 1.379$, class 2 corresponds to run 2 with a lower steady Nu_{ref} of 1.348, and class 3 corresponds to simulations 1, 3 and 5 characterised by oscillatory Nu values with $\overline{Nu} = 1.31$. For Ra = 750, all of the baselines 1–5 are used to initialize the episodes while training the DRL agent, each episode starting from a randomly selected baseline. The resulting \overline{Nu} for Ra = 500 is 1.268 and is used as Nu_{ref} in Eq. (6). For classes 1–3 of Ra = 750, we use the average of all three \overline{Nu} obtained at each of the three classes, obtaining a value of $Nu_{\text{ref}} = 1.346$.

In Fig. 4, we plot the shapes of the convection rolls at the final time step of the baselines. Although training for Ra = 750 is performed with all 5 baseline runs, for brevity, Fig. 4(b) shows the topology for class 3 (run 5) only, since this is the baseline from which the deterministic agent evaluation and proportional control cases are simulated. The topologies of the remaining baseline runs for Ra = 750 are shown in Fig. D3 of Appendix D. At the warmest regions, the v velocities are positive and maximum indicating upward flow, and in the coolest regions, v is negative and minimum indicating flow towards the bottom wall. We define the length scale of the convection rolls as the distance between the warm and cold regions adjacent to each other at points where the temperatures are the maximum and minimum, respectively (*i.e.*, v is maximum and minimum). In both cases, the convection rolls have a length scale of

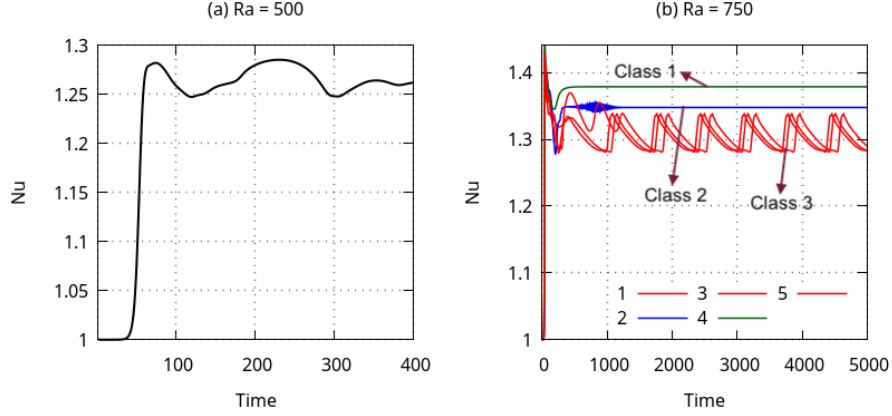


Fig. 3 Baseline simulations showing the evolution of Nu with time t , from the purely conductive no-motion state ($Nu = 1$) to the onset of instability ($Nu > 1$) for (a) $Ra = 500$ and (b) five simulation runs labelled 1–5 for $Ra = 750$ categorized into three classes of baselines.

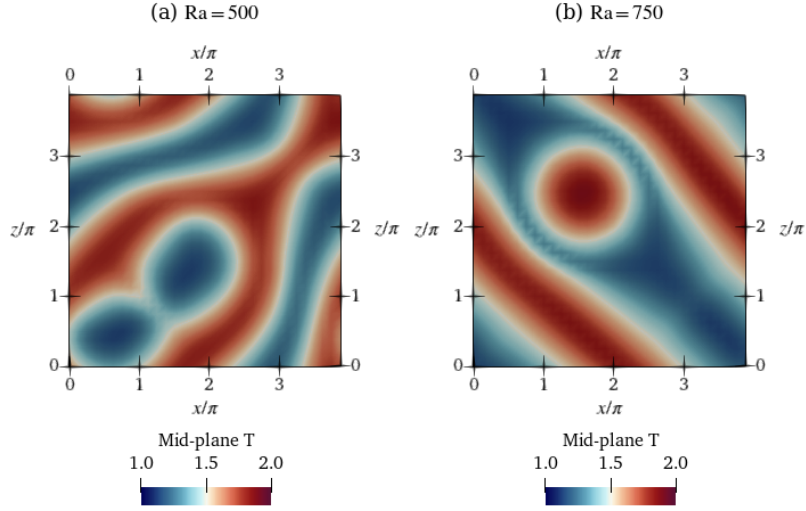


Fig. 4 Temperature fields of the baselines shown in the mid-plane cross-section ($y = 0$) of the domain for (a) $Ra = 500$ at $t = 400$ and (b) for $Ra = 750$ for class 3 (run 5) at time $t = 5000$. Temperature fields of runs 1–4 of the other classes of baselines for $Ra = 750$ are shown in Appendix D. Video files are provided in Online Resource 1 and 2 for $Ra = 500$ and 750 respectively (see Appendix B).

approximately π , an observation in line with results of linear stability analysis (Bergé and Dubois, 1984). We perform a convergence analysis with different simulation time steps Δt to reinforce this result, which further justifies our choice of $\Delta t = 0.1$. The analysis shows that simulations with $\Delta t \leq 0.5$ are reasonable choices of time steps to obtain solutions with length scales of convection rolls that agree with linear stability analysis. Details of the convergence analysis are provided in Appendix A.

Note that videos of the temperature field evolution for these baselines are provided in Online Resource 1 for $Ra = 500$ and Online Resource 2 for $Ra = 750$. Visible from the fields, all baseline shapes for $Ra = 500$ and 750 are irregularly shaped, with no particular spatial pattern. Class 2 and class 3 baselines for $Ra = 750$ exhibit spatial oscillations about a mean shape.

3.2 Training

Figure 5 shows the training curves overlaid with their moving averages, with the horizontal axis being CFD episodes. The plotted values are the Nu averaged over all time steps in each episode. The moving average curves are averaged over a moving window of 20 episodes. In both cases $Ra = 500$ and $Ra = 750$, the mean Nu reduces to values below the Nu_{ref} in the baseline and then remains within a range of values. To measure the final Nu after training, the plotted Nu values are averaged over the last N_E episodes. We denote this final Nu after training as $\langle Nu \rangle_{N_E}$, with $\langle \cdot \rangle_{N_E}$ representing averaging over the last N_E episodes. Thus, in each case, we can quantify the extent of reduction of convection by calculating the percentage decrease of Nu from the reference value Nu_{ref} using the following formula:

$$\text{Percentage reduction of } Nu = \frac{Nu_{\text{ref}} - \langle Nu \rangle_{N_E}}{Nu_{\text{ref}} - 1} \times 100\%. \quad (12)$$

Note that the denominator is $Nu_{\text{ref}} - 1$ and not simply Nu_{ref} . This is because the minimum possible Nu in the RBC system is 1 (Eq. (2) with no convection, *i.e.*, $v=0$) and so the percentage reduction calculation is offset by 1. For $Ra = 500$, $N_E = 50$, (*i.e.*, averaging over episodes 150 to 200) and $\langle Nu \rangle_{N_E} = 1.209$. From the baseline $Nu_{\text{ref}} = 1.268$, this gives is a percentage Nu reduction of 22%.

In Fig. 6, we show the Nu evolution during three episodes in different stages of the training. At episode 25, there is not much improvement compared to Nu_{ref} . However, it is noticeable that the different actuations make the Nu variation more noisy compared to the baseline. At episode 40 and more so at episode 193, a significant improvement is observed. In both cases, the Nu trajectories first drop to a low value between $t = 400 - 450$, and then remain low. In episode 193, the drop to a low Nu occurs sooner ($t = 400 - 410$) and to a much lower value compared to episode 40 ($t = 400 - 450$). This shows that as the training proceeds, the agent learns a more optimal combination of actions to reduce convection more rapidly in the first few timesteps of control, and ensures that the system sustains this controlled state.

In the training curve at $Ra = 750$ in Fig. 5(b), similar to $Ra = 500$, the DRL agent reduces the Nu , showing that a control strategy is learned. However, given that the $Ra = 750$ case is more unstable than $Ra = 500$ and five baselines are used during training, the phase space to be explored by the agent is much larger than for $Ra = 500$, and so learning requires more steps, *i.e.*, a larger number of episodes are required before a significant drop in Nu is observed. The Nu begins to drop at episode 100, compared to episode ≈ 20 for $Ra = 500$. After a gradual decrease in Nu from episode 100–250, it saturates after episode 250. Choosing $N_E = 150$, $\langle Nu \rangle_{N_E} = 1.302$ giving a percentage Nu reduction of 12.7%.

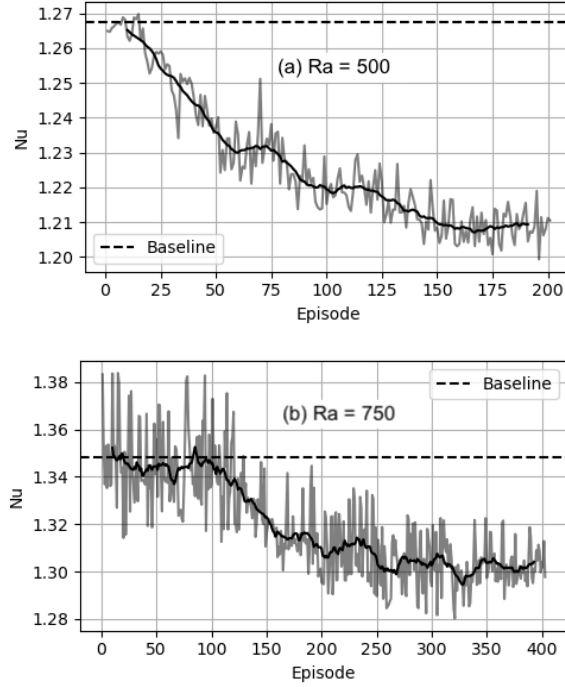


Fig. 5 Training curves for (a) $Ra = 500$ and (b) $Ra = 750$. The episodes on the horizontal axis are CFD episodes. The dashed horizontal lines correspond to Nu_{ref} from the baseline. Grey lines are episode-wise Nu while black lines are for the moving average of Nu over a window of 20 episodes.

In Fig. 7, we plot the Nu evolution during three episodes during the training at $Ra = 750$. Similar to the $Ra = 500$ case, the progress to a more effective control policy is observed for higher episodes. Also similar to $Ra = 500$, during initial times $t < 5020$, the drop in Nu from its initial value is quicker (*i.e.*, a more negative slope) in later episodes compared to earlier ones.

In order to understand the nature of the control policy learned by the agent, we need to investigate the deterministic evaluations of the trained agent, which we show in the next section.

3.3 Deterministic Evaluation

In this section, we get an insight into the control method learned by the agent. In each case $Ra = 500$ and $Ra = 750$, we load the agent saved at the final episodes of the training, *i.e.*, episode 200 for $Ra = 500$ and episode 400 for $Ra = 750$. The loaded agent is used in the evaluation mode, by choosing the most probable action for each observed state in a deterministic manner, in contrast to the training mode, when the agent explored the phase space by using exploration on the actions. In order to compute the percentage reduction in Nu during the deterministic runs, we use the

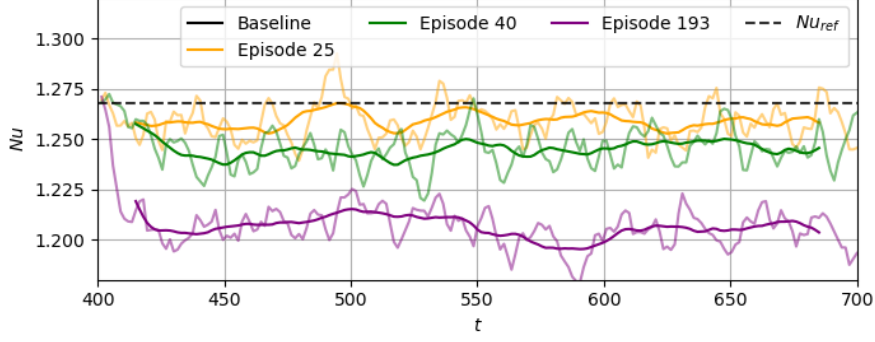


Fig. 6 Evolution of Nu in three episodes during training at $Ra = 500$. Transparent lines represent instantaneous values and bold opaque lines represent the moving-average over 30 time units.

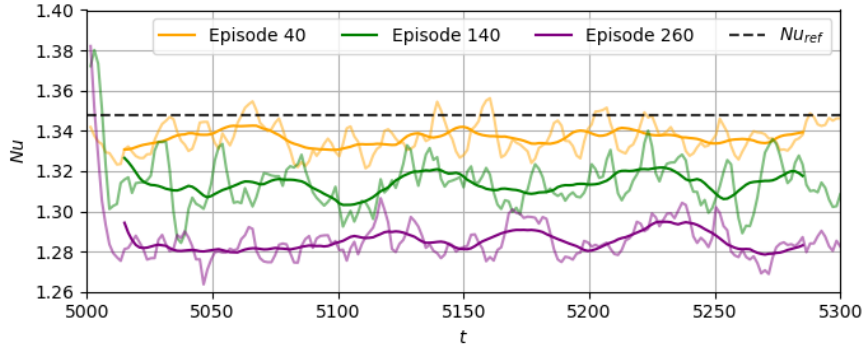


Fig. 7 Evolution of Nu in three episodes during training at $Ra = 750$. Transparent lines represent instantaneous values and bold opaque lines represent the moving-average over 30 time units.

following formula:

$$\text{Percentage reduction of } Nu = \frac{Nu_{\text{ref}} - Nu_C}{Nu_{\text{ref}} - 1} \times 100\%, \quad (13)$$

where $Nu_C = \overline{Nu}^{\Delta t_C}$ is the Nu of the controlled state calculated by averaging the Nu over some portion (Δt_C) of the time during which control is executed. In order to justify the offset by 1 in the denominator, the same reasoning is used as in Eq. (12).

3.3.1 $Ra = 500$

First, we look at the evaluation for $Ra = 500$ in Fig. 8. Control is executed from $t = 400$. Within the first few timesteps, the Nu drops to a low value. Following a period of transients, the system stabilises into a final controlled state from $t = 1300 - 1900$. Thus, $\Delta t_C = 600$ and following Eq. (13), $Nu_C = 1.205$. This corresponds to a Nu reduction of 23.5%.

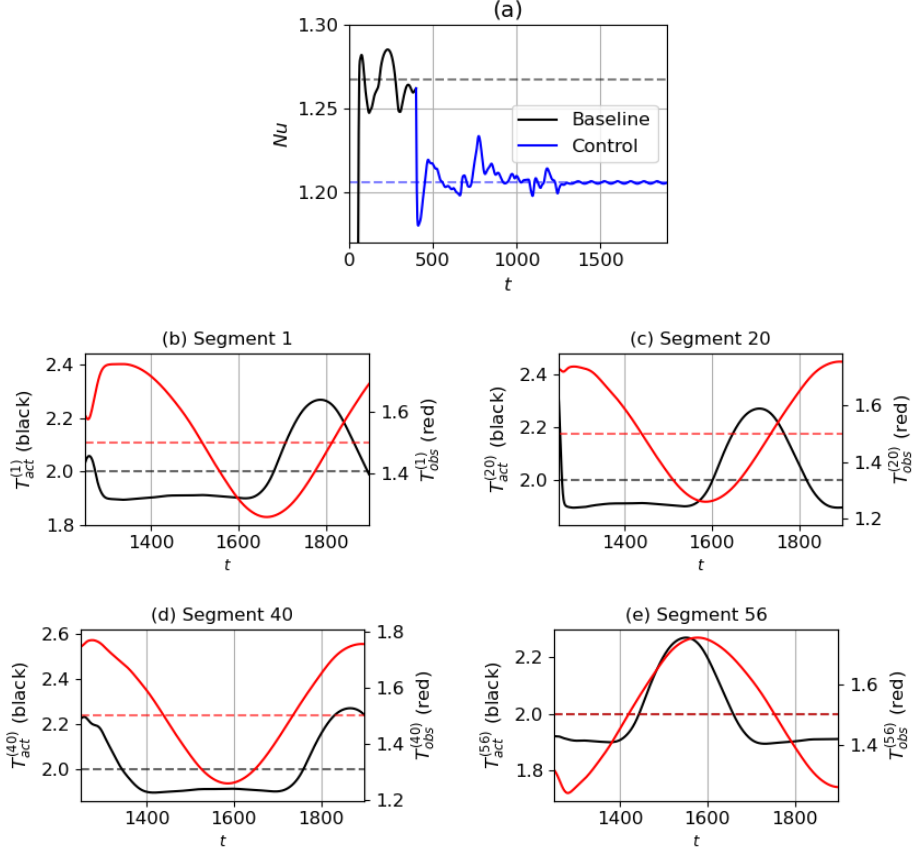


Fig. 8 (a) Nu curve during the deterministic evaluation of the agent at $Ra = 500$, plotted along with the baseline. The broken lines represent Nu_{ref} (black, top) from the baseline, and Nu_C at the controlled state (blue, below). (b)-(e) Evolution of control temperatures $T_{\text{act}}^{(j)}$ (left axis, black lines) and temperature observation at the mid-plane $T_{\text{obs}}^{(j)}$ (right axis, red lines) in randomly selected control segments from $t = 1250 - 1900$. The horizontal broken lines represent the values of $T_{H,0} = 2$ (left axis, black) and 1.5 (right axis, red) respectively.

Next, we show the actions alongside the observations in a few segments in Fig. 8 (b)-(e), to get an idea of the learned policy. Here, segments 1, 20, 40 and 56 are shown for time instants during the final controlled state. In each segment, we compare control temperatures $T_{\text{act}}^{(j)}$ (Eq. (9)) with temperature observations $T_{\text{obs}}^{(j)}$, which are temperatures in the mid-plane $y = 0$ in the j^{th} pseudo-environment averaged in the horizontal directions, *i.e.*, $T_{\text{obs}}^{(j)} = \langle T(x^{(j)}, y = 0, z^{(j)}, t) \rangle_{x^{(j)}, z^{(j)}}$. We also plot in dashed lines the mid-plane temperature at a stable state if there was no convection, which equals 1.5. Noticeably, the control strategy is non-trivial and there exists a complex non-linear relation between the averaged temperature above a segment and the bottom wall temperature chosen by the DRL controller. In particular, we observe:

- **Control actuations disproportionate to observations:** although $T_{\text{obs}}^{(j)}$ are roughly sinusoidal with time, the variation of $T_{\text{act}}^{(j)}$ does not follow the same pattern, but is instead composed of extended periods of actuations below $T_{H,0} = 2$ and short peaks of warmer actuations above $T_{H,0}$. Also, in segments 1 and 20, as T_{obs} increases above 1.5, T_{act} decreases, similar to opposition control. However, T_{act} remains at a low value even when T_{obs} begins to drop. In segments 40 and 56, T_{obs} and T_{act} have the same variation pattern: when T_{obs} decreases below (increases above) the mean, then T_{act} increases above its mean as well. Thus, the learned control strategy features actuations that are disproportionate to the observations in some segments. This is distinct from an opposition control strategy, where the actuations follow a pattern of variation opposite to the observations, uniformly across segments.
- **Differences in actuator delays per segment:** It is also visible from segments 1 and 20 that the T_{act} begins to increase after a short delay in T_{obs} increasing. This duration of delay is different across different segments. In the case of opposition control with delays, $T_{\text{act}}^{(j)}$ would follow the exact opposite pattern of variation as $T_{\text{obs}}^{(j)}$ across segments, and there would be no difference in delays from segment to segment. Moreover in opposition control, the delays in each segment are required to be tuned before the optimal control state is achieved, while in DRL control, these delays are implicitly learned in the control policy.

Next, we show in Fig. 9 how the flow structure corresponding to $\text{Ra} = 500$ is modified by the DRL control compared with that of the baseline (previously shown in Fig. 4). During the transient phase ($t = 400 - 1300$), the DRL controller breaks down the convection rolls in the baseline state into smaller localised blobs (Fig. 9(a)). Then, in the final controlled state beyond $t = 1300$, the structure is rearranged to non-intersecting diagonally running convection rolls (Fig. 9(c)). A sequence of spatial actuation patterns (two of which are shown in Fig. 9(b) and Fig. 9(d)) is executed by the agent in order to modify the flow topology and bring the system to this controlled state. This sequence of actuations is a feature of the learned control policy.

The regular convection structure of the controlled state is representative of RBC at a value of Ra lower than $\text{Ra} = 500$. To demonstrate this, we perform an additional baseline simulation at $\text{Ra} = 400$ and plot its Nu and temperature field in in Fig. 10. $\text{Ra} = 400$ corresponds to a less unstable regime, featuring a smaller convection amplitude compared to $\text{Ra} = 500$, as evident from Fig. 10(a). Further, the temperature field at instability (Fig. 10(b)) shows the regular pattern of diagonal convection rolls. It can thus be stated that the DRL controller modifies the trajectory of the system so that it resembles states observed in more stable regimes.

3.3.2 $\text{Ra} = 750$

We now study the deterministic runs at $\text{Ra} = 750$. We perform evaluations on all the three baseline classes as described in Sec. 3.1, using the latest saved agent from the training of $\text{Ra} = 750$. The results are plotted in Fig. 11. In Fig. 11(a), we see that in all three classes, the agent reduces the Nu to a lower value from the respective baselines. For classes 1 and 2, a controlled state is reached within approximately 200 time units. For class 3, a controlled state is reached within 1000 time units, *i.e.* at time

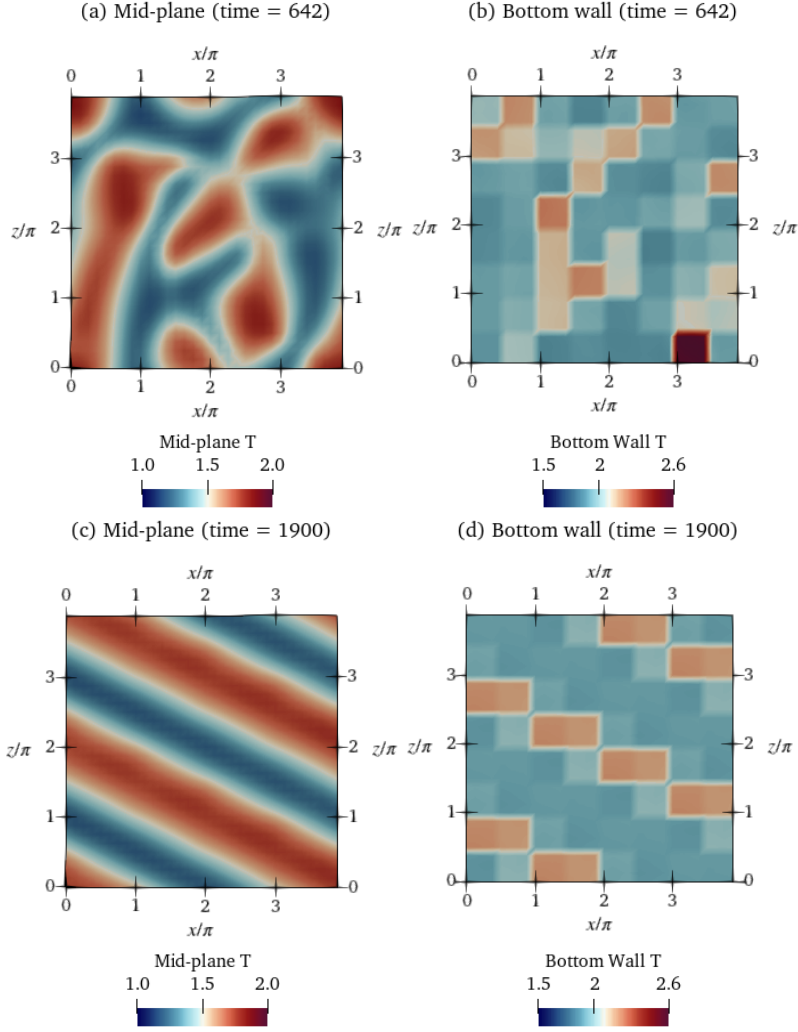


Fig. 9 Deterministic evaluation of the agent at $Ra = 500$: temperature fields during (a)-(b) the transient phase at $t = 642$ and (c)-(d) at the final controlled state at $t = 1900$, shown at two cross-sections - the mid-plane of the domain (a) and (c) and the bottom wall showing the corresponding temperature actuations (b) and (d). Video provided in Online Resource 3.

6000, after a period of transients. In order to calculate the percentage reduction in Nu , the formula in Eq. (13) is used with the Nu_{ref} values being the Nu averaged over the last half of the baselines for each of the classes. As mentioned in Sec. 3.1, this is 1.379, 1.348 and 1.310 respectively for classes 1, 2 and 3. From Fig. 11(a) we calculate the Nu_C reached in each class as 1.312, 1.281 and 1.283 respectively. Therefore, for classes 1, 2 and 3, the agent achieves a percentage of Nu reduction of 17.7%, 19.3% and 8.7%, respectively. Given that the $Ra = 750$ agent is trained on five baselines, the

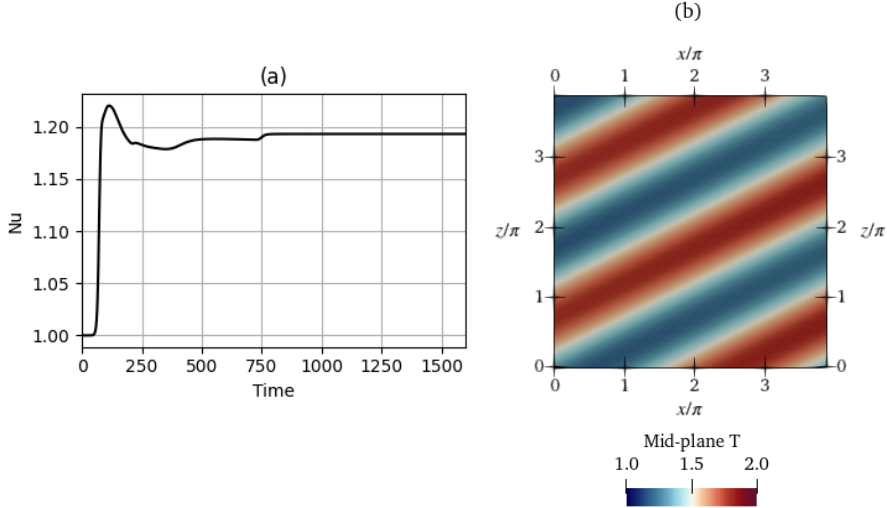


Fig. 10 Evolution of Nu (left) and temperature field at the mid-plane (right) from the baseline simulation at $Ra = 400$. The temperature field is shown corresponding to a time instant of 1500 (video in Online Resource 4).

ability to control all classes of baselines (a wider range of states) is an indicator of the robustness of the DRL agent.

To better understand the learned policy, we observe the plots in 11(c)–(e), where four segments are chosen at random to analyse the action chosen based on the observed states. Opposition control-like relationships are visible in segments 1 and 20, where from $t = 6000 - 7000$, high temperature observations at the mid-plane cause the corresponding actuations to be lower than $T_{H,0} = 2$. However, in segments 40 and 56, an opposite trend is visible. In segment 40 at $t = 6500$, a decrease in T_{obs} is accompanied by a decrease in the actuation temperatures as well, and in segment 56 at $t = 6500$, an increase in T_{obs} is accompanied by an increase in T_{act} . Similar to $Ra = 500$, the delays between the increase/decrease of T_{obs} and increase/decrease of T_{act} are segment-dependent and not consistent across segments, which differentiates the agent-learned control policy from a simple opposition control policy. The qualitative results of the learned control strategy are similar to that observed in $Ra = 500$. The fact that such differences in the policies are observed, while the MARL setup implies that the DRL agent is shared across segments, indicates that complex non-linear strategies that depend on the state in a complex fashion have been chosen by the agent.

Next, we plot the temperature fields of $Ra = 750$ during control in Fig. 12 for the class 3 baseline. As is visible from the plot, the agent breaks down the convection cells in the baseline (previously shown in Fig. 4(b)) into smaller cells, reshaping the structure of the convection to straight rolls running diagonally across the domain. The final controlled state achieved by the agent resembles a convection pattern at a lower, less unstable $Ra = 400$ (Fig. 10).

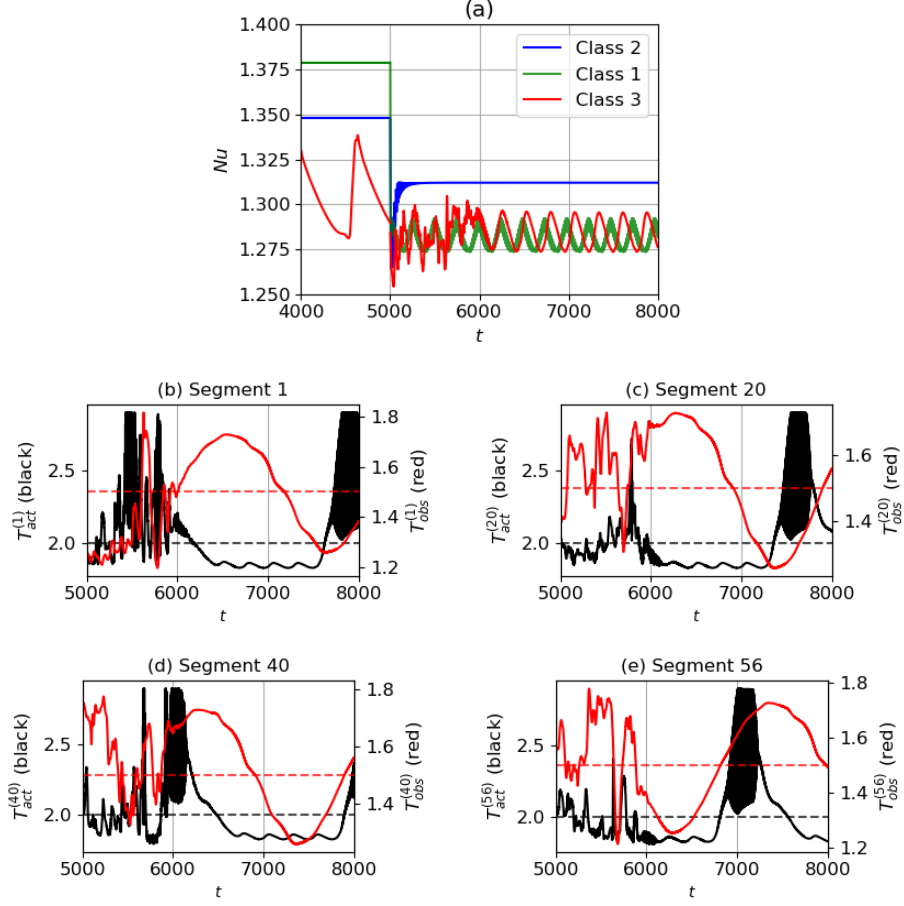


Fig. 11 (a) Evolution of Nu during the deterministic evaluation of the agent at $Ra = 750$, plotted for all three classes of baselines. Control begins at $t = 5000$. (b)–(e) Variation of temperature observation at the mid-plane $T_{\text{obs}}^{(j)}$ (right axis) and control actuation $T_{\text{act}}^{(j)}$ (left axis) in randomly selected control segments.

3.4 Proportional Control

We compare the control policy learned by the DRL agent with a proportional controller applied to the Rayleigh–Bénard system as described in Sec. 2.4. In Figs. 13 and 14, we show the response of the system to proportional control at $Ra = 500$ and $Ra = 750$, respectively. In each case, the simulation is performed starting from the end state of the baseline. For $Ra = 750$, the class 3 baseline is used, since this baseline was used in the deterministic run in Sec. 3.3. In Figs. 13(a) and 14(a), we only show the Nu curves corresponding to the K_p values with the best control performance. In Figs. 13(b) and 14(b), the \overline{Nu} averaged over the last half of the total control time duration is plotted across all K_p . In both Figs. 13 and 14, the mean Nu of the DRL-controlled state, Nu_C is also shown for comparison.

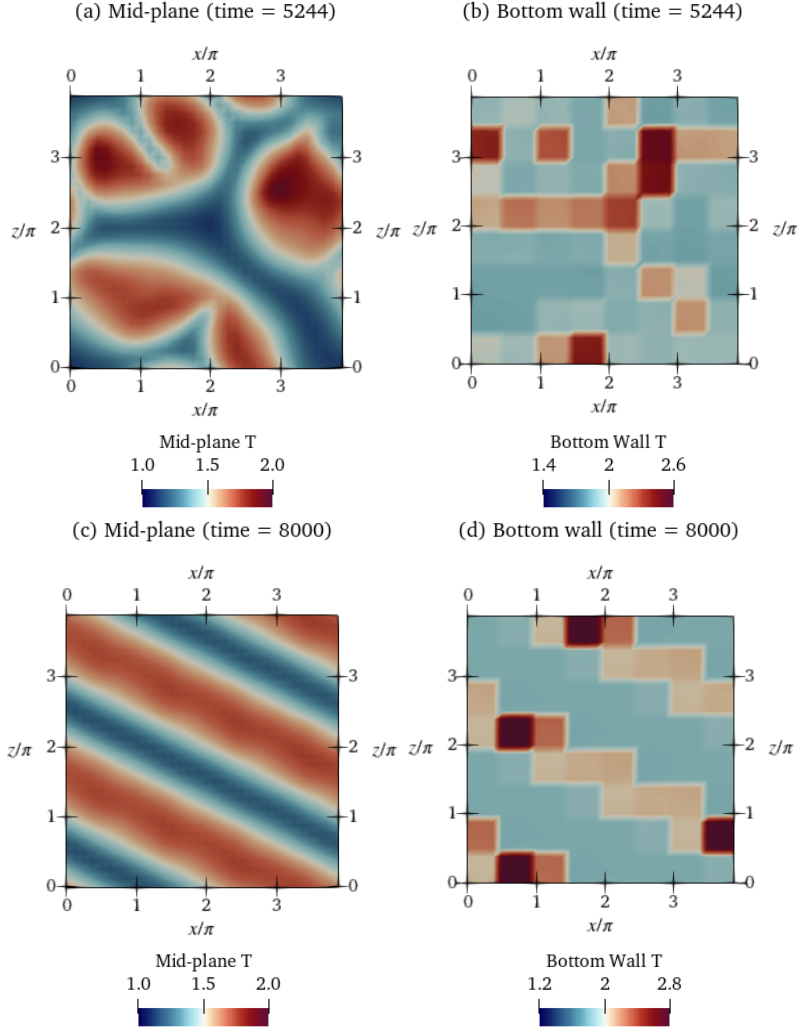


Fig. 12 Deterministic evaluation of the agent at $Ra = 750$ for the class 3 baseline: shown are temperature fields during (a)–(b) the transient phase at $t = 5244$ and (c)–(d) at the final controlled state at $t = 8000$, at two cross-sections - the mid-plane of the domain (a) and (c) and on the bottom wall showing the corresponding temperature actuations (b) and (d). Video in Online Resource 5.

The reduction in Nu for proportional control is computed using Eq. (13). In Fig. 13, $K_p = 0.6$ yields a controlled state with $Nu_C = 1.215$, corresponding to a percent reduction in Nu of 19.8%. This is calculated from the Nu_{ref} for $Ra = 500$ equal to 1.268. A drop in the averaged Nu is observed as the K_p is increased up to 0.6, with either constant Nu , or low-amplitude fluctuations. As K_p is increased beyond 0.6, overshooting occurs: the large control actuations cause the system to become further unstable, and the mean Nu increases. Compared to DRL-based control in Fig. 8(a), the proportional control strategy is sub-optimal even at the best K_p , since DRL-based

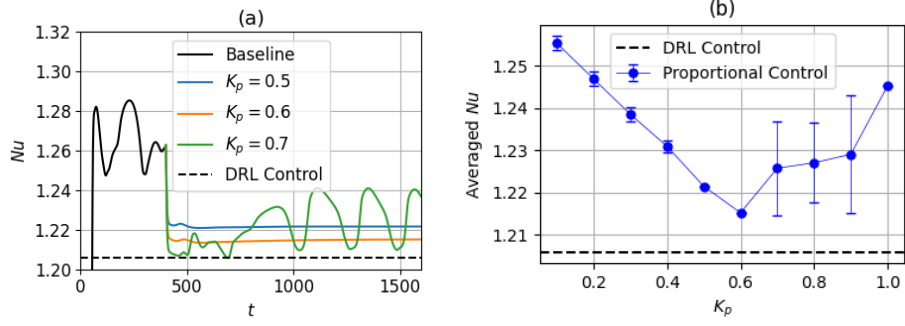


Fig. 13 (a) Time evolution of Nu with proportional control, shown for three different K_p at $Ra = 500$. (b) Time-averaged Nu, averaged over the last half of the total control time duration, shown as a function of K_p . The error bars indicate the standard deviation of the Nu from this averaged value, an indicator of the fluctuation amplitude.

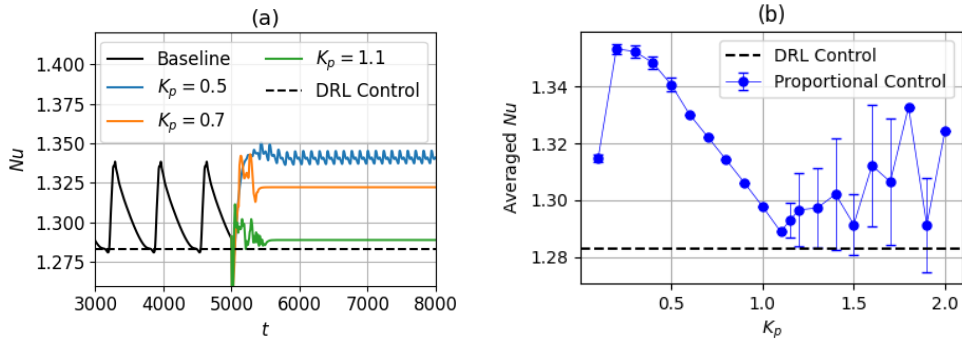


Fig. 14 (a) Time evolution of Nu during proportional control, shown for three different K_p at $Ra = 750$. (b) Time-averaged Nu, averaged over the last half of the total control time duration, shown as a function of K_p . The error bars indicate the standard deviation of the Nu from this averaged value, an indicator of the fluctuation amplitude. The class 3 baseline is used as the starting field.

control reduces the value of Nu to a lower value than the proportional control at $K_p = 0.6$. This result suggests that with DRL, a control policy more sophisticated than a simple proportional control law is discovered. As discussed in Sec. 3.2, this corresponds to additional learned features of the control law such as a range of different actuator delays across segments and actuations disproportionate to temperature observations, corresponding to non-linear DRL control laws.

The temperature field at the final controlled state at $K_p = 0.6$ for $Ra = 500$ is also plotted in Fig. 15. In contrast to the DRL-controlled end state, the convection rolls are not straight and parallel, and do not have uniform thickness, indicating that proportional control is not able to cause the same topological modifications obtained by the non-linear DRL controller.

At $Ra = 750$, as is visible from Fig. 14(a), the K_p corresponding to the largest Nu reduction is 1.1. Similar to $Ra = 500$, the controlled-state mean Nu reduces linearly

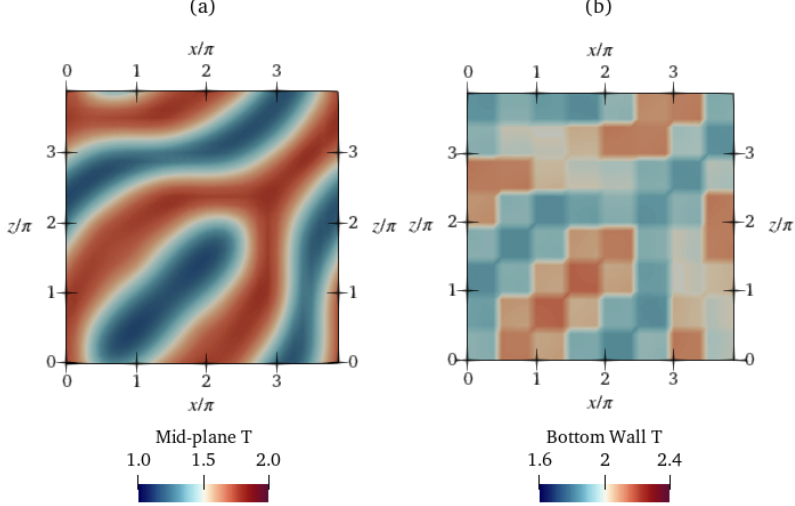


Fig. 15 Temperature field at the (a) mid-plane and (b) bottom wall at $Ra = 500$. The latter shows actuations across control segments for proportional control at $K_p = 0.6$. Video shown in Online Resource 6.

with K_p up to $K_p = 1.1$ with a low-amplitude fluctuation about the mean Nu at each K_p , and beyond 1.1, the mean Nu increases, *i.e.*, overshooting occurs, and the system becomes unstable. A controlled state similar to the DRL-controlled state, with straight parallel cells running diagonally past the domain is observed in Fig. 16. The Nu_C at the controlled state achieved by the DRL agent is 1.283, which is slightly lower than that of the proportional controller at $K_p = 1.1$, which is 1.289. The Nu_{ref} of the class 3 baseline is 1.31 (Sec. 3.1). The DRL controller achieves a percentage Nu reduction of 8.7%, and with proportional control, a 6.8% reduction is achieved.

Although the Nu reduction at $Ra = 750$ using DRL and proportional control are comparable, it is noteworthy that the agent at $Ra = 750$ is trained using three different baselines, and learns an effective control policy for all baselines during a single training run. The agent at $Ra = 750$ is thus more capable to generalise to a wider range of states, highlighting its robustness. In the case of a proportional controller, an efficient tuning of K_p must be carried out for each of the three baseline classes until an optimum Nu reduction is observed.

3.5 Deterministic evaluation in a larger domain

One of the core advantages of MARL compared to SARL is its ability to reduce the state and action space dimensionality by exploiting spatial invariances in the system. This also allows to easily transfer a MARL agent trained on a given domain size to another domain size: as long as the underlying physics are similar, the policy can be applied to a domain of different dimensions by adapting the number of MARL pseudo-environments deployed. In this section, we perform a deterministic run of the agent trained on the 4π -width and -length domain at $Ra = 500$ on a larger domain of size 8π . The number of quadrature points for the CFD solver is doubled in the horizontal

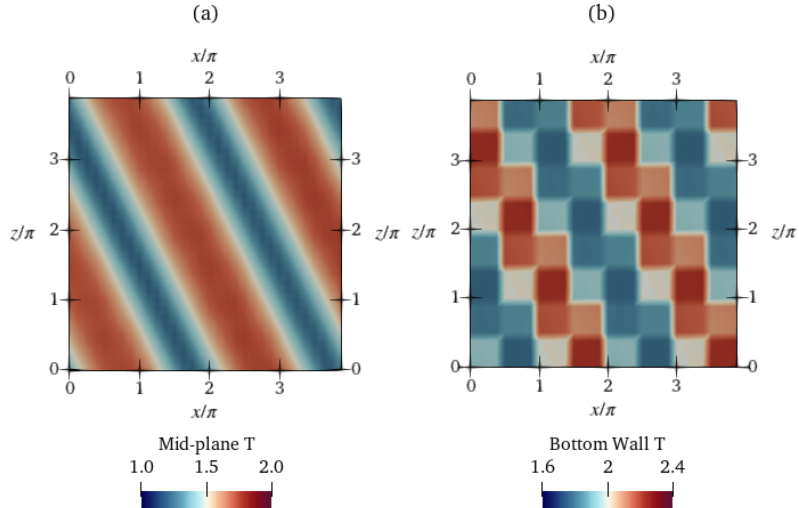


Fig. 16 Temperature field at the (a) mid-plane and (b) bottom wall at $Ra = 750$. The later shows actuations across control segments for proportional control at $K_p = 1.1$. Video shown in Online Resource 7.

directions from $32 \times 16 \times 32$ to $64 \times 16 \times 64$, and the number of control segments is also doubled in each horizontal direction from 8×8 control segments in the 4π domain to 16×16 control segments in the 8π domain. In this way, the size of the input state to each agent is kept constant and each agent observes the same segment size as before, *i.e.*, a segment size of $\pi/2 \times \pi/2$.

We first show the Nu and temperature field of the baseline state in the mid-plane of the 8π domain in Fig. 17. Several curved convection rolls are observed, and the Nu stabilises at a Nu_{ref} (time-averaged over the last half of the baseline time, 5000 to 10000) of 1.246. In Fig. 18 we show the evolution of the Nu of the baseline state and controlled states. By applying the 4π domain-trained agent, the Nu reduces and reaches a mean value of $Nu_C = 1.211$ in the controlled state. Here, Nu_C is computed from $t = 11500$ to the end of the simulation. Using Eq. (13), this is a Nu reduction of 14.2%. Next, we show the flow topology at the mid-plane of the final controlled state in Fig. 19. From the plot, it is visible that the baseline convection rolls are broken and reconfigured to a shape with diagonally running convection rolls that are nearly straight. This pattern is qualitatively similar to the end control states reached by the deterministic evaluation of the agent in $Ra = 500$ and $Ra = 750$ in figures 9(b) and 12(b), respectively, and is topologically closer to the configuration observed at lower Ra (Fig. 10).

4 Conclusion

In the present study, we apply control using deep reinforcement learning (DRL) on a 3D Rayleigh–Bénard convection (RBC) system, as an extension of the work in 2D by Vignon *et al.* (2023). We use the multi-agent reinforcement learning (MARL) framework that involves several agents, each with its own pseudo-environment. Each agent

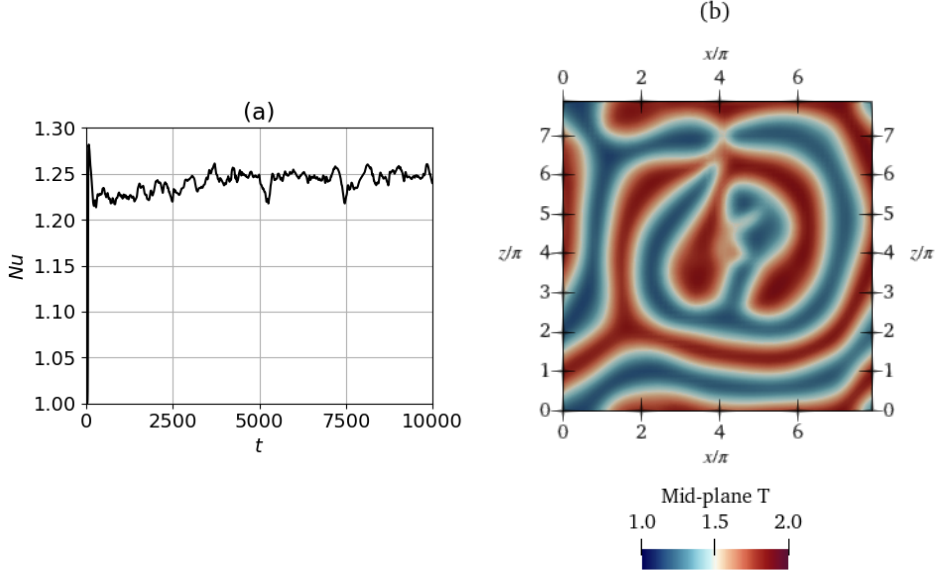


Fig. 17 (a) Nu evolution during the baseline simulation in a domain of size 8π at $Ra = 500$ and (b) corresponding mid-plane temperature field at $t = 10000$ (right). Video of evolution shown in Online Resource 8.

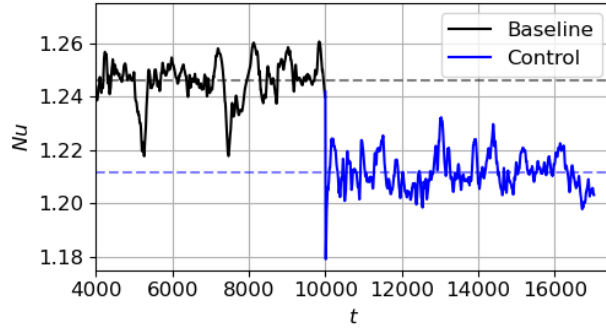


Fig. 18 Evolution of Nu in the 8π domain upon control at $Ra = 500$. The controller used is the agent trained on the 4π domain at $Ra = 500$. The horizontal broken lines represent the mean Nu, averaged over the last half of the duration of the baseline, Nu_{ref} , (black) and over the duration of the control (blue).

has its own stream of state observations and rewards from its corresponding local portion of the domain, and applies an independent control action. MARL is especially beneficial for physical systems such as RBC whose dynamics exhibit spatial translational invariance, and allows to overcome the curse of dimensionality, which is otherwise making trial-and-error learning of distributed output control laws computationally intractable. Compared to the 2D case in [Vignon et al. \(2023\)](#), the larger

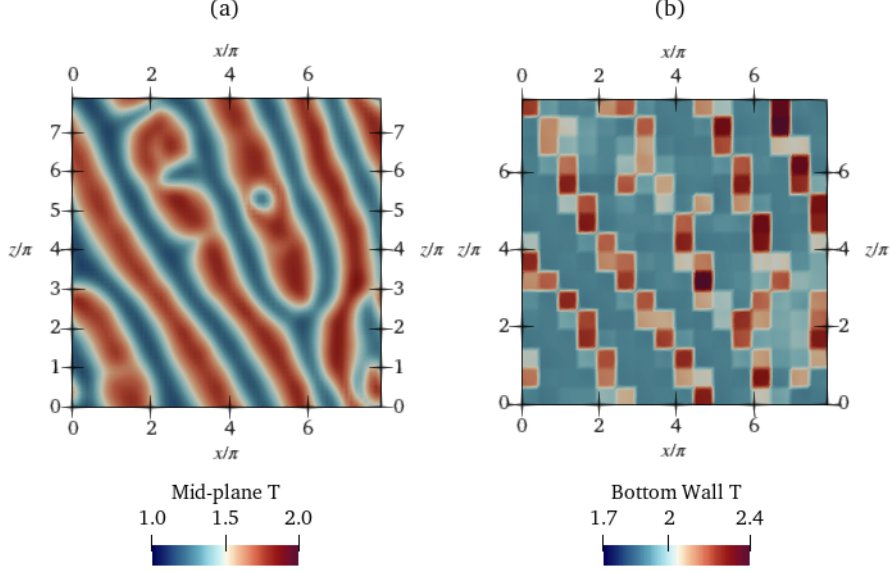


Fig. 19 The temperature field at the mid-plane (a), and control actuations at the bottom wall of the 8π domain (b), obtained from the control executed by the agent trained on the 4π domain. The time of the temperature field corresponds to the final time step in Fig. 18. Video of control shown in Online Resource 9.

control dimensionality (number of actuators required), the larger state space dimensionality and the more complex flow dynamics in the 3D case motivate the need for MARL-based control in 3D. This is, to the best of our knowledge, the first time that DRL control is applied to the 3D RBC system.

The RBC computational domain size is $4\pi \times 2 \times 4\pi$, and the bottom wall is divided into 8×8 square segments of size $0.5\pi \times 0.5\pi$, each of which is assigned to a single MARL agent that applies a temperature value across the segment as its control actuation. Training is performed at $Ra = 500$ and $Ra = 750$. With MARL, control of the RBC system is successfully achieved. During training, the training curves show a drop in Nu by 22% for $Ra = 500$ and 12.7% for $Ra = 750$. Both $Ra = 500$ and $Ra = 750$ are trained with each episode starting from the end state of the baseline for 80% of the total episodes and the remaining 20% starts from the end of the previous episode. In this way, the system also explores trajectories spanning a longer time across successive episodes durations, and thus the agent observes more states, including states representative of the long-term behavior of the system. The case of $Ra = 750$ uses three different classes of baselines with different convective patterns, and hence the trained agent is more robust than if trained using a single baseline. During deterministic evaluation, the agent trained at $Ra = 500$ achieves 23.5% reduction in Nu , and the agent trained at $Ra = 750$ achieves 17.7%, 19.3% and 8.7% Nu reduction on baselines of classes 1, 2 and 3, respectively. The fact that the agent is able to control all three classes of baselines at $Ra = 750$ is an indicator of its robustness. The structure of the convection in the domain is modified upon control from a spatially irregular pattern to straight convection rolls that run diagonally across the domain. The structure of

the convection rolls in the controlled state is topologically similar to that of a RBC system at a lower $Ra = 400$.

Comparisons have also been made with proportional control (PC) using a range of coefficients of proportionality K_p . Results show that the DRL-based control outperforms PC. At $Ra = 500$, PC achieves a 19.8% Nu reduction and at $Ra = 750$, PC achieves a 6.8% reduction, while DRL-based control achieves 23.5% and 8.7%, respectively. Using DRL-based control, in a single training run, the agent learns a more complex control policy than PC, which includes actuator delays and magnitudes of control actions that are different across different segments. As the MARL strategy is adopted in this study, we also show that an agent trained on the 4π domain can be extended in application to control the RBC system at $Ra = 500$ in a domain of a larger size, *i.e.*, 8π -domain. Extending control to larger domains highlights the advantage that MARL can exploit translational invariances of the RBC system at $Ra = 500$.

These results open opportunities for a number of future investigations. Various configurations of agents can be adopted for the control of RBC at larger domains and larger Ra . For example, instead of a single agent having as input the states corresponding to a single segment, a set of multiple neighbouring state segments can be assigned as the input state to a single agent. The input states would then contain information from a larger window of the domain that is influenced by the action imposed in the control segment. We are also working on investigating how the results presented here can be extended to higher Ra cases, in which convection is both stronger and more chaotic. In other flow-control problems, DRL-based control has shown promising results in the turbulent regimes, such as 3D cylinders [Suárez et al. \(2024\)](#), so one could also expect positive results for higher Ra number cases.

DRL-based control has shown promising results in the turbulent regimes for a 3D cylinder, as we see in e.g. flow control for the wake of 3D cylinder ([Suarez et al. 2024](#))

We believe that the present work is an important milestone that takes DRL from simple 2D cases ([Vignon et al., 2023](#)) to complex non-stationary 3D cases. In the future, we will push this further to consider fully turbulent 3D cases, which are relevant for many industrial applications, such as chemical reactors, material manufacturing, and thermal energy systems, where maintaining stable temperature gradients and flow patterns is crucial in order to prevent undesirable instabilities and to enhance efficiency. In other examples such as thermal insulation of buildings, understanding the principles of control in RBC can be crucial to minimize the energy losses of the heating or cooling system.

Acknowledgements. The authors extend their acknowledgement to the National Academic Infrastructure for Supercomputing in Sweden (NAISS) for resources provided for this study, and to the European Research Council (ERC) for financial support. Views and opinions expressed are those of the authors only and do not necessarily reflect those of the European Union or the European Research Council. Neither the European Union nor the granting authority can be held responsible for them.

Declarations

Funding Information. Part of the deep-learning-model training was enabled by resources provided by the National Academic Infrastructure for Supercomputing in Sweden (NAISS). Ricardo Vinuesa acknowledges financial support from ERC grant no. ‘2021-CoG-101043998, DEEPCONTROL’.

Conflict of Interest. The authors declare no conflict of interest.

Author Contributions. Conceptualization: Ricardo Vinuesa, Jean Rabault, Joel Vasanth, Francisco Alcántara-Ávila; Methodology: Ricardo Vinuesa, Jean Rabault, Joel Vasanth, Francisco Alcántara-Ávila; Formal analysis and investigation: Joel Vasanth; Software: Joel Vasanth, Francisco Alcántara-Ávila and Mikael Mortensen; Writing - original draft preparation: Joel Vasanth; Writing - review and editing: Joel Vasanth, Jean Rabault, Francisco Alcántara-Ávila, Mikael Mortensen, Ricardo Vinuesa; Funding acquisition: Ricardo Vinuesa; Resources: Ricardo Vinuesa; Supervision: Jean Rabault, Ricardo Vinuesa, Francisco Alcántara-Ávila. All authors read and approved the final manuscript.

Data Availability. The data that support the findings of this study are available from the corresponding author upon reasonable request.

Appendix A Convergence Analysis

In this section, we simulate the baseline for $Ra = 500$ with different time steps $\Delta t = 0.01, 0.1, 0.2$ and 0.5 in order to justify our choice of $\Delta t = 0.1$. For each Δt , we run five simulations with the same parameters. We note here that for $\Delta t > 0.5$, the solution is found to be numerically unstable and the values of Nu obtained are Nan. Shown in Fig. A1 are the resulting Nu evolutions for $\Delta t \leq 0.5$. We see that in each case, the Nu can reach either a steady or unsteady solution with small fluctuations about the mean. We also note that the mean Nu (averaged from $t = 400 - 1000$) for each of the five simulations for each Δt , lies within the range of 1.23-1.27.

We also observe the flow structures in the temperature fields shown in Fig. A2. The temperature fields for each Δt are from a single randomly selected simulation out of the five solutions, at the end time $t = 1000$. By visual inspection, we note that the convection rolls have a length scale of π that is roughly uniform along the axis of the rolls. Thus, solutions with $\Delta t \leq 0.5$ qualitatively have the same spatial and temporal features, and we deem any of them fit to use as baselines for control.

The thermal relaxation time for the non-dimensional Rayleigh-Bénard problem is $\sqrt{Ra \cdot Pr}$ (Bergé and Dubois, 1984) which for $Ra = 500$ and $Pr = 0.7$ is ≈ 18.7 non-dimensional time units. A motivating factor for selecting $\Delta t = 0.1$ (instead of 0.01 or any value ≤ 0.5) for the remainder of the paper is that this is small enough to be at least 1/100th the thermal relaxation time, and large enough to ensure quicker simulations. Furthermore, during the control simulations, a low Δt ensures that any numerical instabilities that may arise due to the sharp changes in temperature actuations at the bottom wall can be prevented.

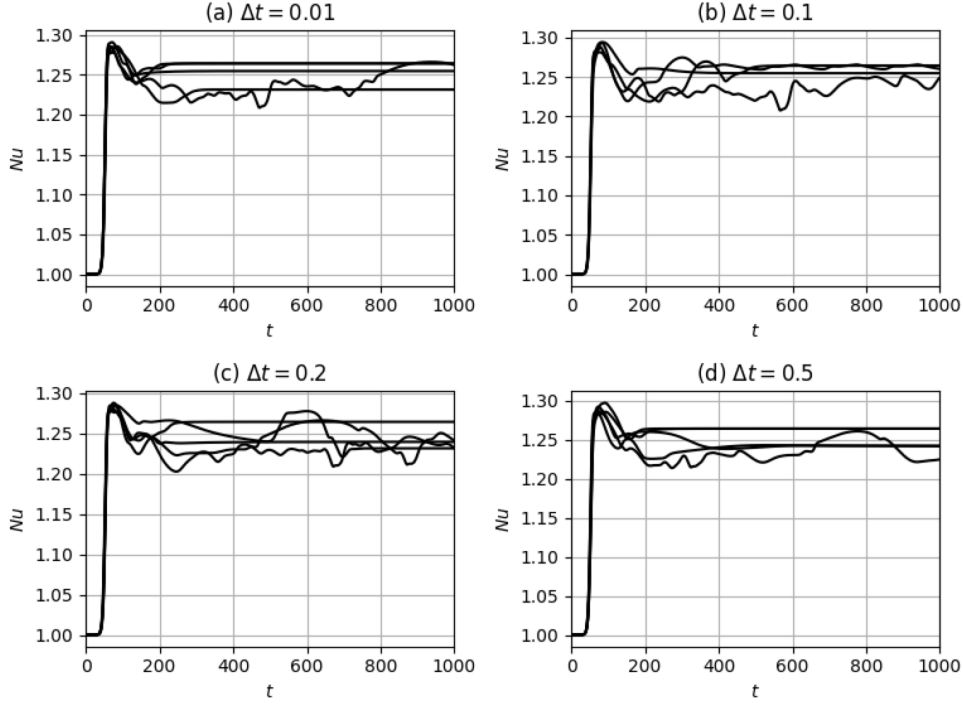


Fig. A1 Time evolutions of Nu with various time steps Δt . For each Δt , five simulations with the same parameters are shown.

Appendix B Supplementary information

Several supplementary files are provided along with this article. These are video animations of temperature-field evolutions from simulation results corresponding to various figures in the main text. An exhaustive list of the video filenames with their captions is provided below. The reader is advised to refer to this list when ‘Online Resource’ is mentioned in the main text. Note that ‘Online Resource’ is abbreviated as ‘OR’ below.

1. OR 1: ‘or1_fig4a_Ra500_baseline.avi’. Mid-plane temperature field evolution of the baseline of $Ra = 500$. Corresponding figure - Fig. 4(a).
2. OR 2: ‘or2_fig4b_Ra750_baseline.avi’. Mid-plane temperature field evolution of the class 3 baseline of $Ra = 750$ (run 5 in Fig. 4(b)).
3. OR 3: ‘or3_fig9_Ra500_det.avi’. Mid-plane and bottom wall temperature fields during the evolution of the RBC system under action of the MARL controller. At time 1300, a more organised regular spatial arrangement of convection rolls is observed, characterised by straight diagonal running cells. Corresponding figure - Fig. 9.
4. OR 4: ‘or4_fig10_Ra400_baseline.avi’. Evolution of the baseline at $Ra = 400$. Time units shown correspond to those in Fig. 10(a).

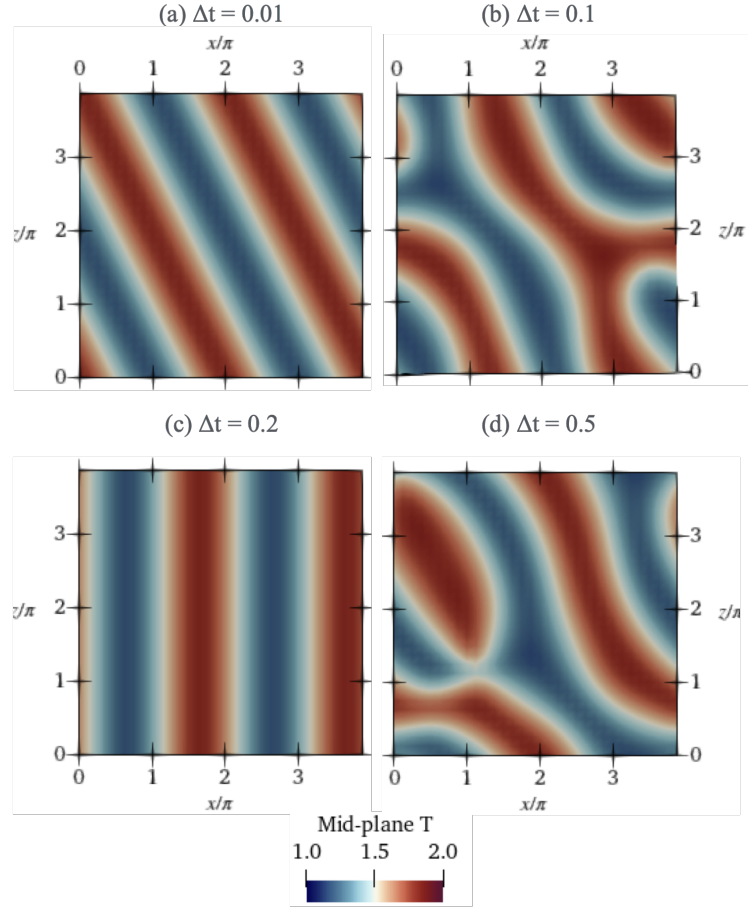


Fig. A2 Mid-plane temperature fields at $t = 1000$ for the simulations with different time steps as shown in Fig. A1.

5. OR 5: 'or5_fig12_Ra750_det.avi'. Deterministic evaluation of agent trained at $Ra = 750$. Irregular baseline shape broken down and convection structure becomes regular, *i.e.*, straight diagonal cells at time 5928. Corresponding figure - Fig. 12
6. OR 6: 'or6_fig15_Ra500_prop_control.avi'. Proportional control for $Ra = 500$ at $K_p = 0.6$. Corresponding figure - Fig. 15.
7. OR 7: 'or7_fig16_Ra750_prop_control.avi'. Proportional control for $Ra = 750$ at $K_p = 1.1$. Corresponding figure - Fig. 16.
8. OR 8: 'or8_fig17_Ra500_8pi_baseline.avi'. Baseline evolution for $Ra = 500$ in a domain of length 8π . Corresponding figure - Fig. 17.
9. OR 9: 'or9_fig19_Ra500_det_8pi_control.avi'. MARL agent trained on domain of length 4π used in deterministic evaluation mode for the control of RBC in larger domain of length 8π . Corresponding figure - Fig. 19.

Appendix C Open source code release on Github

All the codes, scripts, and post-processing tools used in this work will be made available on Github together with readmes and user instructions, over publication of this manuscript. Reasonable user support will be provided through the issue tracker of the corresponding Github repository. The url for the repository is https://github.com/KTH-FlowAI/DRL_MARL_RayleighBenard3D_Control.

The shenfun CFD case setup is described in great details, including all the numerical implementation considerations, elements chosen, and code walk-through, on the shenfun RBC documentation page: <https://shenfun.readthedocs.io/en/latest/rayleighbenard.html>. Note that the conventions used in the present paper and in this documentation page are slightly different: while the present paper uses x as the horizontal (“wall parallel”) description and y as the vertical (“wall normal”) direction, the documentation page uses the opposite conventions. This has no influence on the CFD results *per se*. The code uses the same conventions as the shenfun documentation, and only the present paper uses separate conventions, for simplicity of the writing and conformity with the literature.

Appendix D Convection structure for $Ra = 750$ baselines

In this appendix, we show the temperature fields for the baselines for $Ra = 750$ (not shown in Fig. 4(b)) as described in Sec. 3.1.

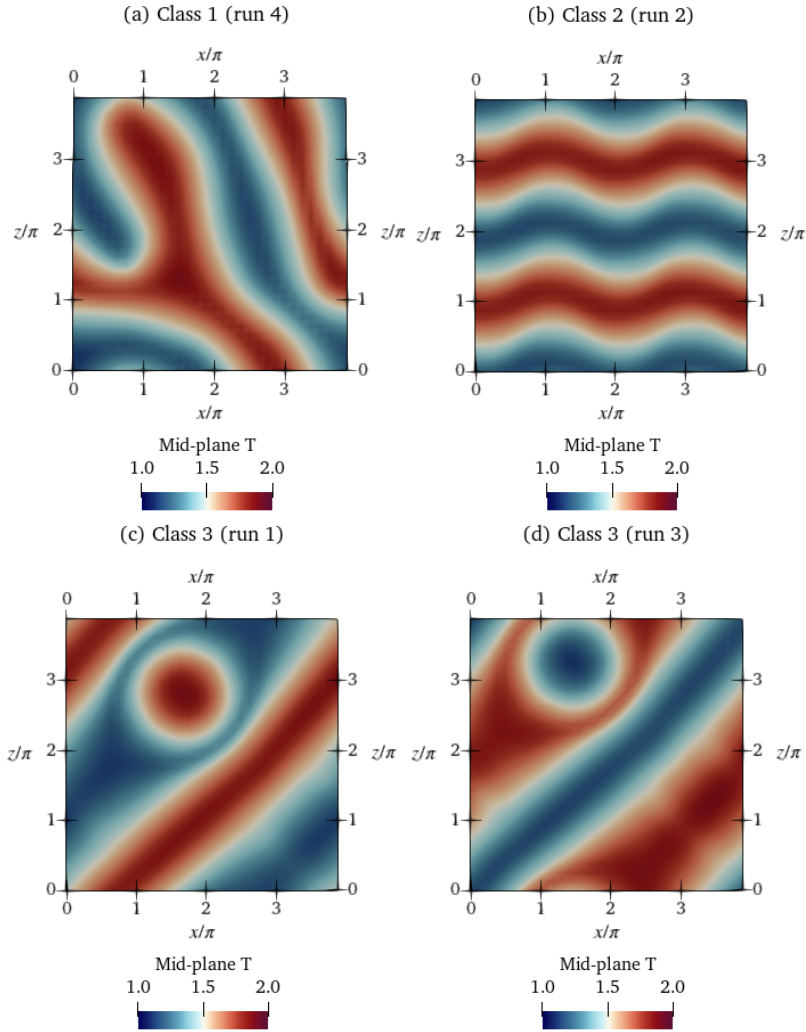


Fig. D3 Temperature fields of the baselines shown in the mid-plane cross-section ($y = 0$) of the domain for $Ra = 750$ for (a) Class 1 (b) Class 2. (c-d) runs 1 and 3 of class 3 (Fig. 3). Run 5 of class 3 is shown in Fig. 4(b).

References

- Alnæs, M., Blechta, J., Hake, J., Johansson, A., Kehlet, B., Logg, A., Richardson, C., Ring, J., Rognes, M.E., Wells, G.N.: The fenics project version 1.5. *Archive of numerical software* **3**(100) (2015)
- Ascher, U.M., Ruuth, S.J., Spiteri, R.J.: Implicit-explicit runge-kutta methods for time-dependent partial differential equations. *Applied Numerical Mathematics* **25**(2), 151–167 (1997) [https://doi.org/10.1016/S0168-9274\(97\)00056-1](https://doi.org/10.1016/S0168-9274(97)00056-1)
- Beintema, G., Corbetta, A., Biferale, L., Toschi, F.: Controlling Rayleigh–Bénard convection via reinforcement learning. *Journal of Turbulence* **21**(9-10), 585–605 (2020)
- Bergé, P., Dubois, M.: Rayleigh–Bénard convection. *Contemporary Physics* **25**(6), 535–582 (1984) <https://doi.org/10.1080/00107518408210730>
- Bae, H.J., Koumoutsakos, P.: Scientific multi-agent reinforcement learning for wall-models of turbulent flows. *Nature Communications* **13**(1), 1443 (2022) <https://doi.org/10.1038/s41467-022-28957-7>
- Brunton, S.L., Noack, B.R.: Closed-loop turbulence control: Progress and challenges. *Applied Mechanics Reviews* **67**(5), 050801 (2015)
- Brunton, S.L., Noack, B.R., Koumoutsakos, P.: Machine learning for fluid mechanics. *Annual review of fluid mechanics* **52**(1), 477–508 (2020)
- Belus, V., Rabault, J., Viquerat, J., Che, Z., Hachem, E., Reglade, U.: Exploiting locality and translational invariance to design effective deep reinforcement learning control of the 1-dimensional unstable falling liquid film. *AIP Advances* **9**(12), 125014 (2019)
- Bucci, M.A., Semeraro, O., Allauzen, A., Wisniewski, G., Cordier, L., Mathelin, L.: Control of chaotic systems by deep reinforcement learning. *Proceedings of the Royal Society A* **475**(2231), 20190351 (2019)
- Chevalier, M.: Adjoint based control and optimization of aerodynamic flows. PhD thesis, *Mécanik* (2002)
- Carbo, R.M., Smith, R.W.M., Poese, M.E.: A computational model for the dynamic stabilization of Rayleigh–Bénard convection in a cubic cavity. *The Journal of the Acoustical Society of America* **135**(2), 654–68 (2014)
- Chen, W., Wang, Q., Yan, L., Hu, G., Noack, B.R.: Deep reinforcement learning-based active flow control of vortex-induced vibration of a square cylinder. *Physics of Fluids* **35**(5) (2023)
- Degrave, J., Felici, F., Buchli, J., Neunert, M., Tracey, B., Carpanese, F., Ewalds, T.,

- Hafner, R., Abdolmaleki, A., Las Casas, D., *et al.*: Magnetic control of tokamak plasmas through deep reinforcement learning. *Nature* **602**(7897), 414–419 (2022)
- Drazin, P.G., Reid, W.H.: *Thermal Instability*. Cambridge Mathematical Library, pp. 32–68. Cambridge University Press, London (2004)
- Albrecht, S.V., Christianos, F.: Schäfer, L.: *Multi-Agent Reinforcement Learning: Foundations and Modern Approaches*. pp. 3–12. MIT Press, (2024)
- Font, B., Alcántara-Ávila, F., Rabault, J., Vinuesa, R., Lehmkuhl, O.: Active flow control of a turbulent separation bubble through deep reinforcement learning. In: *Journal of Physics: Conference Series*, vol. 2753, p. 012022 (2024). IOP Publishing
- Fan, D., Yang, L., Wang, Z., Triantafyllou, M.S., Karniadakis, G.E.: Reinforcement learning for bluff body active flow control in experiments and simulations. *Proceedings of the National Academy of Sciences* **117**(42), 26091–26098 (2020)
- Getling, A.V.: *Rayleigh-benard Convection: Structures And Dynamics*. World Scientific Publishing Co Pte Ltd, London (1998)
- Guadarrama, S., Korattikara, A., Ramirez, O., Castro, P., Holly, E., Fishman, S., Wang, K., Gonina, E., Wu, N., Kokiopoulou, E., Sbaiz, L., Smith, J., Bartók, G., Berent, J., Harris, C., Vanhoucke, V., Brevdo, E.: *TF-Agents: A library for Reinforcement Learning in TensorFlow* (2018). <https://github.com/tensorflow/agents>
- Guastoni, L., Rabault, J., Schlatter, P., Azizpour, H., Vinuesa, R.: Deep reinforcement learning for turbulent drag reduction in channel flows. *The European Physical Journal E* **46**(4), 27 (2023) <https://doi.org/10.1140/epje/s10189-023-00285-8>
- Garnier, P., Viquerat, J., Rabault, J., Larcher, A., Kuhnle, A., Hachem, E.: A review on deep reinforcement learning for fluid mechanics. *Computers & Fluids* **225**, 104973 (2021)
- Howle, L.E.: Active control of Rayleigh–Bénard convection. *Physics of Fluids* **9**, 1861 (1997)
- Jasak, H., Jemcov, A., Tukovic, Z., *et al.*: Openfoam: A C++ library for complex physics simulations. In: *International Workshop on Coupled Methods in Numerical Dynamics*, vol. 1000, pp. 1–20 (2007). Dubrovnik, Croatia)
- Kelly, R.E.: Stabilization of Rayleigh–Bénard convection by means of a slow nonplanar oscillatory flow. *Physics of Fluids A: Fluid Dynamics* **4**, 647 (1992)
- Kim, J., Moin, P., Moser, R.: Turbulence statistics in fully developed channel flow at low Reynolds number. *Journal of Fluid Mechanics* **177**, 133–166 (1987) <https://doi.org/10.1017/S0022112087000892>

- Kuhnle, A., Schaarschmidt, M., Fricke, K.: Tensorforce: a tensorflow library for applied reinforcement learning. Web page **9** (2017)
- Kuhnle, A., Schaarschmidt, M., Fricke, K.: Tensorforce: a TensorFlow library for applied reinforcement learning. Web page (2017). <https://github.com/tensorforce/tensorforce>
- Li, J., Zhang, M.: Reinforcement-learning-based control of confined cylinder wakes with stability analyses. *Journal of Fluid Mechanics* **932**, 44 (2022)
- Mnih, V., Kavukcuoglu, K., Silver, D., Graves, A., Antonoglou, I., Wierstra, D., Riedmiller, M.: Playing atari with deep reinforcement learning. arXiv preprint arXiv:1312.5602 (2013)
- Mortensen, M.: Shenfun: High performance spectral Galerkin computing platform. *Journal of Open Source Software* **3**(31), 1071 (2018) <https://doi.org/10.21105/joss.01071>
- Mortensen, M.: Shenfun's documentation : <https://shenfun.readthedocs.io>. Web page (2018). <https://shenfun.readthedocs.io/en/latest/index.html>
- Novati, G., Laroussilhe, H.L., Koumoutsakos, P.: Automating turbulence modelling by multi-agent reinforcement learning. *Nature Machine Intelligence* **3**(1), 87–96 (2021) <https://doi.org/10.1038/s42256-020-00272-0>
- Or, A.C., Speyer, J.L.: Active suppression of finite-amplitude Rayleigh–Bénard convection. *Journal of Fluid Mechanics* **483**, 111–128 (2003)
- Paris, R., Beneddine, S., Dandois, J.: Robust flow control and optimal sensor placement using deep reinforcement learning. *Journal of Fluid Mechanics* **913**, 25 (2021)
- Paris, R., Beneddine, S., Dandois, J.: Reinforcement-learning-based actuator selection method for active flow control. *Journal of Fluid Mechanics* **955**, 8 (2023)
- Pino, F., Schena, L., Rabault, J., Mendez, M.A.: Comparative analysis of machine learning methods for active flow control. *Journal of Fluid Mechanics* **958**, 39 (2023)
- Pandey, A., Scheel, J.D., Schumacher, J.: Turbulent superstructures in Rayleigh–Bénard convection. *Nature Communications* **9**, 2118 (2018)
- Rabault, J., Kuhnle, A.: Accelerating deep reinforcement learning strategies of flow control through a multi-environment approach. *Physics of Fluids* **31**(9), 094105 (2019)
- Rabault, J., Kuchta, M., Jensen, A., Réglade, U., Cerardi, N.: Artificial neural networks trained through deep reinforcement learning discover control strategies for active flow control. *Journal of fluid mechanics* **865**, 281–302 (2019)

- Ren, F., Rabault, J., Tang, H.: Applying deep reinforcement learning to active flow control in weakly turbulent conditions. *Physics of Fluids* **33**(3), 037121 (2021)
- Rabault, J., Ren, F., Zhang, W., Tang, H., Xu, H.: Deep reinforcement learning in fluid mechanics: A promising method for both active flow control and shape optimization. *Journal of Hydrodynamics* **32**, 234–246 (2020)
- Ren, F., Wang, C., Tang, H.: Active control of vortex-induced vibration of a circular cylinder using machine learning. *Physics of Fluids* **31**(9), 093601 (2019)
- Ren, F., Wang, C., Tang, H.: Bluff body uses deep-reinforcement-learning trained active flow control to achieve hydrodynamic stealth. *Physics of Fluids* **33**(9), 093602 (2021)
- Remillieux, M.C., Zhao, H., Bau, H.H.: Suppression of Rayleigh-Bénard convection with proportional-derivative controller. *Physics of Fluids* **19**, 017102 (2007)
- Ren, F., Zhang, F., Zhu, Y., Wang, Z., Zhao, F.: Enhancing heat transfer from a circular cylinder undergoing vortex induced vibration based on reinforcement learning. *Applied Thermal Engineering* **236**, 121919 (2024)
- Suárez, P., Alcántara-Ávila, F., Miró, A., Rabault, J., Font, B., Lehmkuhl, O., Vinuesa, R.: Active flow control for three-dimensional cylinders through deep reinforcement learning (2023) [arXiv:2309.02462](https://arxiv.org/abs/2309.02462)
- Singer, J., Bau, H.H.: Active control of convection. *Physics of Fluids A: Fluid Dynamics* **3**, 2859 (1991)
- Sutton, R.S., Barto, A.G.: *Reinforcement Learning: An Introduction* (second Edition). MIT press, Cambridge, Massachusetts (2018)
- Swaminathan, A., Garrett, S.L., Poesse, M.E., Smith, R.W.M.: Dynamic stabilization of the Rayleigh-Bénard instability by acceleration modulation. *The Journal of the Acoustical Society of America* **144**, 2334 (2018)
- Silver, D., Hubert, T., Schrittwieser, J., Antonoglou, I., Lai, M., Guez, A., Lanctot, M., Sifre, L., Kumaran, D., Graepel, T., *et al.*: A general reinforcement learning algorithm that masters chess, shogi, and go through self-play. *Science* **362**(6419), 1140–1144 (2018)
- Silver, D., Lever, G., Heess, N., Degris, T., Wierstra, D., Riedmiller, M.: Deterministic policy gradient algorithms. In: *International Conference on Machine Learning*, pp. 387–395 (2014)
- Sonoda, T., Liu, Z., Itoh, T., Hasegawa, Y.: Reinforcement learning of control strategies for reducing skin friction drag in a fully developed channel flow. *arXiv preprint arXiv:2206.15355* (2022)

- Shen, J., Tang, T., Wang, L.-L.: Spectral Methods - Algorithms, Analysis and Applications. Springer, Heidelberg (2011)
- Schulman, J., Wolski, F., Dhariwal, P., Radford, A., Klimov, O.: Proximal policy optimization algorithms. arXiv preprint arXiv:1707.06347 (2017)
- Suárez, P., Alcántara-Ávila, F., Miró, A., Rabault, J., Font, B., Lehmkuhl, O., Vinuesa, R.: Active flow control for drag reduction through multi-agent reinforcement learning on a turbulent cylinder at $Re_D = 3900$ (2024). <https://arxiv.org/abs/2405.17655>
- Tang, J., Bau, H.H.: Stabilization of the no-motion state in Rayleigh-bénard convection through the use of feedback control. Phys. Rev. Lett. **70**, 1795–1798 (1993) <https://doi.org/10.1103/PhysRevLett.70.1795>
- Tang, H., Rabault, J., Kuhnle, A., Wang, Y., Wang, T.: Robust active flow control over a range of Reynolds numbers using an artificial neural network trained through deep reinforcement learning. Physics of Fluids **32**(5), 053605 (2020)
- Vinyals, O., Babuschkin, I., Czarnecki, W.M., Mathieu, M., Dudzik, A., Chung, J., Choi, D.H., Powell, R., Ewalds, T., Georgiev, P., *et al.*: Grandmaster level in starcraft II using multi-agent reinforcement learning. Nature **575**(7782), 350–354 (2019)
- Van Hasselt, H., Guez, A., Silver, D.: Deep reinforcement learning with double q-learning. In: Proceedings of the AAAI Conference on Artificial Intelligence, vol. 30 (2016)
- Vinuesa, R., Lehmkuhl, O., Lozano-Durán, A., Rabault, J.: Flow control in wings and discovery of novel approaches via deep reinforcement learning. Fluids **7**(2), 62 (2022)
- Verma, S., Novati, G., Koumoutsakos, P.: Efficient collective swimming by harnessing vortices through deep reinforcement learning. Proceedings of the National Academy of Sciences of the United States of America **115**(23), 5849–5854 (2018) <https://doi.org/10.1073/pnas.1800923115> . Accessed 2023-01-03
- Vignon, C., Rabault, J., Vinuesa, R.: Recent advances in applying deep reinforcement learning for flow control: Perspectives and future directions. Physics of Fluids **35**(3), 031301 (2023) <https://doi.org/10.1063/5.0143913>
- Vignon, C., Rabault, J., Vasanth, J., Alcántara-Ávila, F., Mortensen, M., Vinuesa, R.: Effective control of two-dimensional Rayleigh-Bénard convection: Invariant multi-agent reinforcement learning is all you need. Physics of Fluids **35**(6), 065146 (2023) <https://doi.org/10.1063/5.0153181>

- Varela, P., Suárez, P., Alcántara-Ávila, F., Miró, A., Rabault, J., Font, B., García-Cuevas, L.M., Lehmkuhl, O., Vinuesa, R.: Deep reinforcement learning for flow control exploits different physics for increasing Reynolds number regimes. In: *Actuators*, vol. 11, p. 359 (2022). MDPI
- Wang, Y.Z., Singer, J., Bau, H.H.: Controlling chaos in a thermal convection loop. *J. Fluid Mech.* **237**, 479 (1992)
- Wang, Q., Yan, L., Hu, G., Li, C., Xiao, Y., Xiong, H., Rabault, J., Noack, B.R.: Drlinfluids: An open-source python platform of coupling deep reinforcement learning and openfoam. *Physics of Fluids* **34**(8) (2022)
- Wang, Q., Yan, L., Hu, G., Chen, W., Rabault, J., Noack, B.R.: Dynamic feature-based deep reinforcement learning for flow control of circular cylinder with sparse surface pressure sensing. *Journal of Fluid Mechanics* **988**, 4 (2024)
- Xu, D., Zhang, M.: Reinforcement-learning-based control of convectively unstable flows. *Journal of Fluid Mechanics* **954**, 37 (2023)
- Xu, H., Zhang, W., Deng, J., Rabault, J.: Active flow control with rotating cylinders by an artificial neural network trained by deep reinforcement learning. *Journal of Hydrodynamics* **32**(2), 254–258 (2020)
- Yan, L., Li, Y., Hu, G., Chen, W.-l., Zhong, W., Noack, B.R.: Stabilizing the square cylinder wake using deep reinforcement learning for different jet locations. *Physics of Fluids* **35**(11) (2023)